Manuscript accepted for publication
Publication is available in open access, see https://doi.org/10.2514/1.J063417

Harmonic Turbulent Stress Budgets in Forced Transonic Flow over a Bump

Nicolas Goffart * and Benoît Tartinville †
Cadence Design Systems Belgium
Chaussée de la Hulpe 189, Brussels B-1170, Belgium

Sergio Pirozzoli ‡
Sapienza University of Rome
via Eudossiana 18, 00184 Rome, Italy

The transonic flow over a bump is studied using implicit large-eddy simulations. To replicate rotor/stator interactions occurring in turbomachinery, harmonic forcing of the back pressure is imposed at the outlet. Various perturbation frequencies are prescribed and encompass different regimes, from a fully locked configuration to a decoupling between the unperturbed and forced flows. The mean solution is however found to be independent of the perturbation. In a triple decomposition framework, the coherent component of the flow is extracted by phase-averaging. Organized structures of streamwise velocity and turbulence kinetic energy are highlighted. Whereas of similar shapes beneath the shock system, their extent in the downstream boundary layer is controlled by the frequency of the perturbation. Mean and harmonic turbulent stress budgets are presented. A typical three-peaks distribution of mean turbulent diffusion is reported, which is also found to appear for the coherent turbulent diffusion. Harmonic production arises mainly from the mean shear and its modulation.

Nomenclature

a	=	speed of sound [m s^{-1}]
A	=	amplitude
B_h, B_l	=	bump height, bump length [m]
C_f	=	friction coefficient
C_p	=	pressure coefficient
C_{uu}	=	streamwise velocity correlation coefficient
C_T	=	artificial viscosity scaling factor

*PhD Student, ngoffart@cadence.com
†Software Architect, tartin@cadence.com
‡Professor, Department of Mechanical and Aerospace Engineering, sergio.pirozzoli@uniroma1.it

d	=	distance from the wall [m]
D_{ij}	=	dissipation tensor [m^2s^{-3}]
e	=	specific internal energy [m^2s^{-2}]
f	=	frequency [s^{-1}]
f_r	=	reduced frequency
h	=	specific enthalpy [m^2s^{-2}]
$I_x,\ I_y,\ I_z$	=	turbulence length scales [m]
$J_{ij,k}$	=	diffusion flux tensor [m^2s^{-3}]
k	=	turbulence kinetic energy [m^2s^{-2}]
$L_x,\ L_y,\ L_z$	=	domain dimensions [m]
M	=	Mach number
N_{bl}	=	number of blocks for Welch method
p	=	pressure [kg $m^{-1}s^{-2}$]
P_{ij}	=	production tensor [m^2s^{-3}]
q_i	=	heat flux vector [kg s^{-3}]
Re	=	Reynolds number
s_0	=	shock sensor threshold
s_{ij}	=	strain-rate tensor [s^{-1}]
$s_{D,0}$	=	Ducros sensor threshold
St	=	Strouhal number
t	=	time [s]
T	=	temperature [K], period [s]
T_{ij}	=	pressure strain tensor [m^2s^{-3}]
u, v, w	=	velocity in x, y and z directions [m s^{-1}]
U	=	mean streamwise velocity [m s^{-1}]
x, y, z	=	spatial coordinates [m]
β	=	directional parameter
δ_0	=	reference boundary layer thickness [m]
δ_{ij}	=	Kronecker delta
$\Delta x, \Delta y, \Delta z$	=	grid resolutions [m]
θ	=	boundary layer momentum thickness [m]
κ	=	shock sensor range

λ	=	thermal conductivity [kg m^{2}s^{-3}K^{-1}]
μ	=	dynamic viscosity [kg m^{-1}s^{-1}]
ν	=	kinematic viscosity [m^{2}s^{-1}]
ν_T	=	kinematic eddy viscosity [m^{2}s^{-1}]
ρ	=	density [kg m^{-3}]
σ_{ij}	=	viscous stress tensor [kg m^{-1}s^{-2}]
τ	=	penalty parameter
ϕ	=	phase angle [°]

Subscripts

i, j, k	=	index notation
o	=	outlet
w	=	wall
∞	=	free stream

Superscripts

$\bar{}$	=	mean component
$\tilde{}$	=	coherent (harmonic) component
$'$	=	incoherent component
$^+$	=	wall unit

I. Introduction

In many high-speed aeronautical applications, the shock wave/boundary layer interaction is the primary aerodynamic performance-limiting factor. For instance, the operation of turbomachines in the transonic regime leads to the development of a shock wave in the passage that interacts with the boundary layer on the suction side of the blade. For strong interactions, the boundary layer separates and a massive recirculation appears, amplified by the blade curvature. The oscillation of the back pressure produced by the periodic passage of a downstream rotating row further affects the interaction and the turbulence in the separated region. The unsteady potential effect of this rotor/stator interaction is enhanced as modern designs tend toward more compact engines and taking it into account at the design stage would allow an improvement in engine efficiency.

Industry relies mostly on low-fidelity methods to design turbomachines. Besides Reynolds-Averaged Navier-Stokes (RANS) simulations and their unsteady counterpart (URANS), frequency-domain approaches such as the Non-Linear Harmonic (NLH) method (originally described in He and Ning [1] and implemented in commercial software by Vilmin et al. [2]) or the Harmonic Balance [3] method are also employed. These methods indeed benefit from a drastically

reduced cost with respect to full unsteady computations thanks to the inherent periodicity of turbomachinery flows. The closure of the harmonic equations derived in the NLH framework requires, however, a model for the harmonic turbulent stresses, the assumptions of which can, in some cases, degrade the accuracy of the solution [4]. The development of better models would improve the predictions given by harmonic methods and widen their range of application.

Any modeling work is based on a good understanding of the underlying physics and consequently on reliable data. The complex phenomena featured in transonic turbomachinery flows necessitate the use of high-fidelity approaches including Large-Eddy Simulation (LES) or Direct Numerical Simulation (DNS) to be appropriately captured [5]. Despite their increasing affordability and popularity, high-fidelity simulations remain costly. One remedy is to consider simpler geometries that, when suitable flow conditions are chosen, replicate most of the actual flow. For example, two-dimensional bumps can be used to perform fundamental flow physics investigation instead of a three-dimensional blade.

The study of transonic flow over two-dimensional bumps dates back to the experimental works of Delery [6] and Liu and Squire [7]. The flow conditions and bump geometry of the latter study were employed by Sandham et al. [8] to demonstrate the feasibility of high-fidelity simulations for the fully turbulent transonic flow over a bump. The Reynolds number based on the bump length and free stream conditions $\mathrm{Re}_{B_l} = B_l U_\infty / \nu$ was $\approx 2.3 \times 10^5$, around 7 times lower compared to the experiment. The boundary layer was found to separate over the bump much earlier than in the experiment, the peak Mach number was lower, and the results featured a steady shock. Bron [9] specifically designed a new bump to study basic flow interactions in turbomachinery and conducted both experiments and (U)RANS numerical investigations. Other authors employed high-fidelity methods on this bump. Wollblad et al. [10] presented the results of LES for which the conditions were similar to the experiment with the exception again of the Reynolds number which had to be decreased by a factor of 11.25 to make the computation feasible, giving $\mathrm{Re}_{B_l} \approx 3.1 \times 10^5$. No natural large-scale movement of the shock was observed. The effects of flow conditions and computational setup on the shock motion were further examined in Wollblad et al. [11], in order to rule out possible explanations for the absence of shock motion. Four additional cases were introduced, with different combinations of domain height, outlet pressure and type of top boundary condition to examine the influence of choked/non-choked flow and/or elliptic leakage along the ceiling. The results showed again the absence of large-scale shock motion, although its innermost part was found to oscillate in some cases. Brouwer [12] performed a DNS but at a higher Mach number (0.79 against 0.7 in Bron [9]) and at an even lower Reynolds number ($\mathrm{Re}_{B_l} \approx 1.7 \times 10^5$). Motion of the lower part of the shock was highlighted at low frequency. More recently, laminar and turbulent interactions in a transonic passage were studied by Priebe et al. [13] using wall-resolved implicit LES (ILES) on a custom geometry.

The budget of turbulence kinetic energy was analyzed in detail by Marquillie et al. [14] and Laval and Marquillie [15] from DNS data of incompressible turbulent flow in a converging-diverging channel, previously studied experimentally by Bernard et al. [16]. The Reynolds number Re_τ (based on the friction velocity and half the channel height) was

decreased by an order of magnitude, from $\mathrm{Re}_\tau \approx 6500$ in the experiment to $\mathrm{Re}_\tau \approx 395$ and $\mathrm{Re}_\tau \approx 617$ in the DNS. No shock was found to to form, but the simulations still featured flow separation at the bump wall. A complex modification of the balance in the adverse pressure gradient region was highlighted. In particular, turbulent transport was found to have a significant influence in the presence of flow separation. Schiavo et al. [17] reported the results from LES for the same configuration, at $\mathrm{Re}_\tau \approx 615$ and $\mathrm{Re}_\tau \approx 950$. Budgets for each individual turbulent stress were portrayed and illustrated that their respective contribution to the turbulence kinetic energy budget varies along the wall. The turbulence kinetic energy budget was further investigated in Schiavo et al. [18] by means of Proper Orthogonal Decomposition and spectral analysis. Turbulent transport was shown to be poorly reconstructed when only the most energetic flow modes are considered.

Work was also done on forced transonic flow over a bump. Bur et al. [19] performed an experimental and numerical study, using URANS. The perturbation was imposed downstream as a periodic pressure signal. The forcing frequencies investigated were low, such that the flow was quasi-steady. A phase lag between the core flow and the boundary layer was observed in the region downstream of the shock, but not in the shock oscillation region. Moroianu et al. [20] reported the results of ILES on the same geometry, and observed the occurrence of a hysteresis cycle, during which the shock system can vary significantly. Investigations of forced oscillations were also performed by Bron [9], again both experimentally and by the means of URANS simulations. The perturbation frequency reached up to 500Hz (or 1000Hz for the numerical study), giving a relatively high reduced frequency $f_\mathrm{r} = f B_\mathrm{l}/U_\infty \approx 0.4$. This order of magnitude is also encountered in turbomachinery flows [21] and means that convection and periodic fluctuations are two equally dominant mechanisms. A high-fidelity simulation related to that geometry was performed by Bodin and Fuchs [22]. However, the reduced frequencies were one or two order(s) of magnitude lower. None of these studies reported a detailed analysis of the influence of the forcing on the turbulent stresses.

In this paper, wall-resolved ILES of the transonic flow over the bump of Bron [9] are employed. An unperturbed configuration and three cases with different realistic forcing frequencies are considered and compared. The effect of the forced conditions on the shock motion, the wall pressure and the separation bubble is assessed. The harmonic (coherent) component of the flow is extracted using a phase-averaging procedure. Emphasis is given on the coherent turbulence kinetic energy and the detailed budgets of mean and coherent turbulent stresses. Besides a clearer understanding of the forced flow, the objective of the study is to provide better insights for turbulence modelers working in the framework of frequency-domain methods. The paper is structured as follows. In section II, the governing equations are introduced and the triple decomposition adopted for the harmonic analysis is presented. The high-order solver is then described and the flow conditions are specified for the various cases in section III. The results are analyzed in section IV, first for the unperturbed case, and then for all the forced cases. Finally, some conclusions are drawn in section V.

II. Governing Equations

A. Compressible Navier-Stokes equations

The compressible Navier-Stokes equations are, using the convention of repeated indices, given by

$$\frac{\partial \rho}{\partial t} + \frac{\partial}{\partial x_i}(\rho u_i) = 0 \tag{1a}$$

$$\frac{\partial}{\partial t}(\rho u_i) + \frac{\partial}{\partial x_j}(\rho u_i u_j) = -\frac{\partial p}{\partial x_i} + \frac{\partial \sigma_{ij}}{\partial x_j} \tag{1b}$$

$$\frac{\partial}{\partial t}\left[\rho\left(e + \frac{1}{2}u_i u_i\right)\right] + \frac{\partial}{\partial x_j}\left[\rho u_j\left(h + \frac{1}{2}u_i u_i\right)\right] = \frac{\partial}{\partial x_j}(u_i \sigma_{ij}) + \frac{\partial q_j}{\partial x_j} \tag{1c}$$

The viscous stress tensor σ_{ij} and heat flux vector q_i are defined following, respectively, the Newtonian and Fourier constitutive relations,

$$\sigma_{ij} = 2\mu\left(s_{ij} - \frac{1}{3}\frac{\partial u_k}{\partial x_k}\delta_{ij}\right) \tag{2}$$

$$q_i = -\lambda\frac{\partial T}{\partial x_i} \tag{3}$$

with s_{ij} the instantaneous strain-rate tensor. The molecular viscosity μ is computed using Sutherland's law.

B. Triple decomposition for incompressible flows

To extract and analyze the harmonic component of the flow, the triple decomposition of Reynolds and Hussain [23] is adopted. Any instantaneous quantity a can be written as the sum of three components,

$$a(x, y, z, t; T) = \overline{a}(x, y, z) + \widetilde{a}(x, y, z, t/T) + a'(x, y, z, t) \tag{4}$$

where $\overline{a}$ is the mean component, $\widetilde{a}$ is the coherent (also called periodic or harmonic) component and a' is the incoherent (or random) component. Both the coherent and incoherent components depend on time but, for this decomposition to be meaningful, their time scales must differ by several orders of magnitude. Typically, the coherent component is related to a single low frequency, whereas the incoherent component corresponds to broadband phenomena at higher frequencies. This criterion will be detailed later in the flow conditions section.

In this work, the main focus is on the turbulent stresses $u'_i u'_j$, to which the triple decomposition can also be applied. The influence of the low-frequency periodic forcing on the turbulence is quantified through the coherent turbulent stress $\widetilde{u'_i u'_j}$, obtained from

$$\widetilde{u'_i u'_j} = \langle u'_i u'_j \rangle - \overline{u'_i u'_j} \tag{5}$$

with $\langle u'_i u'_j \rangle$ the phase average and $\overline{u'_i u'_j}$ the usual Reynolds stress. The transport equations for the mean and coherent components of turbulent stresses can be derived as well and, following [24], can be re-organized to highlight the

contributions of production P_{ij}, pressure strain T_{ij}, dissipation D_{ij} and diffusion flux $J_{ij,k}$. For the mean, it leads to

$$\overline{u_k}\frac{\partial\overline{u_i'u_j'}}{\partial x_k} + \overline{\widetilde{u_k}\frac{\partial\widetilde{u_i'u_j'}}{\partial x_k}} = \overline{P}_{ij} + \overline{T}_{ij} - \overline{D}_{ij} - \overline{J}_{ij,k} \tag{6}$$

with

$$\overline{P}_{ij} = -\left(\overline{u_j'u_k'}\frac{\partial\overline{u_i}}{\partial x_k} + \overline{u_i'u_k'}\frac{\partial\overline{u_j}}{\partial x_k} + \overline{\widetilde{u_j'u_k'}\frac{\partial\widetilde{u_i}}{\partial x_k}} + \overline{\widetilde{u_i'u_k'}\frac{\partial\widetilde{u_j}}{\partial x_k}}\right) \tag{7a}$$

$$\overline{T}_{ij} = \frac{1}{\rho}\left(\overline{p'\frac{\partial u_i'}{\partial x_j}} + \overline{p'\frac{\partial u_j'}{\partial x_i}}\right) \tag{7b}$$

$$\overline{D}_{ij} = 2\nu\overline{\frac{\partial u_i'}{\partial x_k}\frac{\partial u_j'}{\partial x_k}} \tag{7c}$$

$$\overline{J}_{ij,k} = \overline{J}^T_{ij,k} + \overline{J}^p_{ij,k} + \overline{J}^\nu_{ij,k} \tag{7d}$$

and in which the three contributions to the diffusive flux include turbulent, pressure and viscous terms, given by, respectively,

$$\overline{J}^T_{ij,k} = \frac{\partial}{\partial x_k}\left(\overline{u_i'u_j'u_k'}\right) \tag{8a}$$

$$\overline{J}^p_{ij,k} = \frac{\partial}{\partial x_k}\left(\frac{1}{\rho}\overline{u_j'p'}\delta_{ik} + \frac{1}{\rho}\overline{u_i'p'}\delta_{jk}\right) \tag{8b}$$

$$\overline{J}^\nu_{ij,k} = -\frac{\partial}{\partial x_k}\left(\nu\frac{\partial\overline{u_i'u_j'}}{\partial x_k}\right) . \tag{8c}$$

As a consequence of the triple decomposition, additional contributions appear in the convection and production terms compared to the transport equations arising from the typical Reynolds decomposition. For the coherent turbulent stress, the transport equation is given by

$$\frac{\partial\widetilde{u_i'u_j'}}{\partial t} + \overline{u_k}\frac{\partial\widetilde{u_i'u_j'}}{\partial x_k} + \overline{\widetilde{u_k}\frac{\partial\widetilde{u_i'u_j'}}{\partial x_k}} = \widetilde{P}_{ij} + \widetilde{T}_{ij} - \widetilde{D}_{ij} - \widetilde{J}_{ij,k} \tag{9}$$

with

$$\widetilde{P}_{ij} = -\left(\widetilde{u_i'u_k'}\frac{\partial\widetilde{u_j}}{\partial x_k} - \overline{\widetilde{u_i'u_k'}\frac{\partial\widetilde{u_j}}{\partial x_k}} + \overline{u_i'u_k'}\frac{\partial\widetilde{u_j}}{\partial x_k} + \widetilde{u_i'u_k'}\frac{\partial\overline{u_j}}{\partial x_k}\right)$$
$$-\left(\widetilde{u_j'u_k'}\frac{\partial\widetilde{u_i}}{\partial x_k} - \overline{\widetilde{u_j'u_k'}\frac{\partial\widetilde{u_i}}{\partial x_k}} + \overline{u_j'u_k'}\frac{\partial\widetilde{u_i}}{\partial x_k} + \widetilde{u_j'u_k'}\frac{\partial\overline{u_i}}{\partial x_k}\right) \tag{10a}$$

$$\widetilde{T}_{ij} = \frac{1}{\rho}\left(\widetilde{p'\frac{\partial u_i'}{\partial x_j}} + \widetilde{p'\frac{\partial u_j'}{\partial x_i}}\right) \tag{10b}$$

$$\widetilde{D}_{ij} = 2\nu\widetilde{\frac{\partial u_i'}{\partial x_k}\frac{\partial u_j'}{\partial x_k}} \tag{10c}$$

$$\widetilde{J}_{ij,k} = \widetilde{J}^T_{ij,k} + \widetilde{J}^p_{ij,k} + \widetilde{J}^\nu_{ij,k} \tag{10d}$$

and turbulent diffusion, pressure diffusion and viscous diffusion are, respectively,

$$\widetilde{J}^T_{ij,k} = \frac{\partial}{\partial x_k}\left(\widetilde{u_i'u_j'u_k'}\right) \tag{11a}$$

$$\widetilde{J}^p_{ij,k} = \frac{\partial}{\partial x_k}\left(\frac{1}{\rho}\widetilde{u_j'p'}\delta_{ik} + \frac{1}{\rho}\widetilde{u_i'p'}\delta_{jk}\right) \tag{11b}$$

$$\widetilde{J}^\nu_{ij,k} = -\frac{\partial}{\partial x_k}\left(\nu\widetilde{\frac{\partial u_i'u_j'}{\partial x_k}}\right). \tag{11c}$$

All the terms are essentially the same, with the exception of the coherent production, which contains twice more contributions compared to the mean production.

Note that the flow has been assumed to be incompressible when deriving these equations. As the flow is transonic, the density variation across the viscous layer is relatively low and compressibility effects are expected to be small. The validity of this assumption will be repeatedly checked a-posteriori.

III. Computational Methodology

A. Flow solver

The compressible Navier-Stokes equations are solved using an in-house high-order solver. The discretization of the spatial derivatives is based on the flux reconstruction (FR) approach, introduced by Huynh [25]. A particular nodal Discontinuous Galerkin method is recovered as the correction functions chosen are the left and right Radau polynomials. The solution points are the Gauss points. Roe's approximate Riemann solver [26] is employed to compute the common advective fluxes whereas the common solutions and common diffusive fluxes are evaluated using the Local Discontinuous Galerkin approach [27] with $\beta = 0$ and $\tau = 1$ [28]. No subgrid-scale model is considered, that is to say the present simulations are implicit LES. The energy dissipation from the smallest turbulent scales is left to

the numerical scheme itself. The temporal derivative is computed with a 5-stages fourth-order low-storage explicit Runge-Kutta scheme [29].

To deal with shock wave/boundary layer interactions, an efficient shock-capturing technique has to be used. In this work, the Laplacian artificial viscosity method of Persson and Peraire [30] is combined with the Ducros sensor [31]. This additional step is required to discriminate the shock from the boundary layer and ensures that artificial viscosity is focused around shocks only. Details about the implementation can be found in Goffart et al. [32]. Besides shock-capturing, the robustness is further enhanced by the use of a positivity-preserving limiter [33].

Turbulent fluctuations are introduced at the inlet as a boundary condition and are generated with the digital filtering method. Instead of the original 3D filter implementation [34], the approach of a 2D filter composed of the directions tangent to the inlet plane is adopted. The filter is from inception a 2D filter and not a convolution of two 1D filters [35], making the approach valid for unstructured grids. This 2D slice is then correlated in time with the previous time step following [36]. Velocity perturbations are finally scaled according to Lund's transformation [37].

The solver was validated for canonical oblique shock wave reflection on a turbulent boundary layer [32].

B. Flow conditions and simulation setup

The case under investigation is the transonic flow over a bump, the geometry of which is taken from the experiment of Bron [9]. The bump length B_l is 0.184m and its thickness B_h is 10.48mm, whereas the wind tunnel height L_y is 0.12m. The upstream conditions are a total pressure of 160kPa, a total temperature of 300K and a Mach number of 0.7. The ratio $\rho_\mathrm{w}/\rho_\infty$ is around 0.9 and is close enough to unity to assume that compressibility effects in the boundary layer are negligible, as also assumed by Sartor et al. [38]. The mean outlet static pressure is 106kPa, so that a shock wave develops in the rear part of the bump, promoting flow separation. Various cases will be considered in this work depending on the way the back pressure evolves in time. The case with steady back pressure ($A_{\widetilde{p}_\mathrm{o}} = 0$) will be referred to as the baseline case. Then, three cases with sinusoidally varying back pressure will be presented. In the context of turbomachinery, this perturbation mimics the potential effect of a rotor/stator interaction [39]. The amplitude is fixed at 2% of the mean ($A_{\widetilde{p}_\mathrm{o}}/\overline{p}_\mathrm{o} = 0.02$) and the frequency is either 250Hz, 500Hz or 1000Hz. The triple decomposition is valid since one period at the forcing frequency is in the worst case 4×10^{-3}s whereas the characteristic time scale of the energetic eddies in the incoming turbulent boundary layer is $O(\delta_0/U_\infty) \approx 3.8 \times 10^{-5}$s. The Reynolds number based on the bump length amounts to $\approx 1.9 \times 10^5$, which is 20 times lower in comparison to the experiment. The fluid is air assumed as a perfect gas but with a dynamic viscosity multiplied by the same factor.

The computational domain is a rectangular box with the bump geometry as bottom boundary. With respect to the bump, the beginning of which is located at $x = 0$m, the domain extends from $30\delta_0$ upstream to $20\delta_0$ downstream. In the spanwise direction, the domain is $4\delta_0$ wide. Following the experimental measurements of Sigfrids [40], the reference boundary layer thickness δ_0 is here 8.95mm, measured at $x = -0.1$m. This was also considered in other numerical

studies [10].

The mesh consists of hexahedra. Using the high-order FR approach, the target grid resolution is evaluated by considering a uniform distribution of the solution points within the cells, here with polynomial order three. In the streamwise direction, the grid spacing is initially constant, with $\Delta x^+ = 16$, in wall units based on the upstream conditions. Over the last $10\delta_0$, the mesh is progressively coarsened to $\Delta x^+ = 160$ to dampen high-frequency reflected waves. In the spanwise direction, $\Delta z^+ = 12$. The mesh is stretched in the wall-normal direction. Bottom and top boundary layers comprise 100 solution points each, the first one targeting $y^+ = 1$. The exact distribution of the solution points leads in fact to $y_w^+ \approx 0.28$. From the edge of the boundary layers and in the free stream, $\Delta y^+ = 16$. The total number of degrees of freedom rises to approximately 80 million.

The inlet boundary is subsonic, with total pressure, total temperature and velocity direction imposed. These profiles, as well as Reynolds stress profiles (needed for the turbulent inflow), are taken from the averaged solution of a precursor ILES of a turbulent boundary layer in the same flow conditions. Turbulence length scales are $I_x/\delta_0 = 0.5$, $I_z/\delta_0 = 0.375$ and I_y is varying in the wall-normal direction such that $I_y = I_z$ at the edge of the boundary layer and the number of neighbors in the filter is practically constant. The top and bottom boundaries are no-slip adiabatic walls and periodic boundary conditions are imposed in the spanwise direction. A spatially constant static pressure is imposed along the fully subsonic outlet boundary.

The explicit time step is 4×10^{-8}s and corresponds to a Courant-Friedrichs-Lewy (CFL) number of around 2.5. The parameters of the shock-capturing technique (see Goffart et al. [32]) are s_0 = -4.5, κ = 1.5, C_T = 0.01 and $s_{D,0}$ = 0.2. Density is used as the sensor variable.

The simulation is first restarted from an initial RANS solution for a duration of around 45 convective time units (1 CTU = B_l/U_∞) to set up the flow for the baseline case. For the forced cases, the perturbation is then applied for 30 additional CTUs so that the periodic flow can develop. The duration of the transient phases was checked to be sufficiently long by monitoring the shock location at its mid-height. The data extraction starts after the transient phase(s). All the cases are run over the same physical time which corresponds to exactly 10 periods at 500Hz or approximately 25 CTUs. Each computation employed 960 central processing units (CPU) and the estimated cost rises to around 8500 CPUh/CTU.

C. Data acquisition and reduction

The data for this study are collected, after the transient phase(s), every 50 iterations at the bump wall and on a slice at mid-span. Both instantaneous data and instantaneous span-averaged data are available. The latter is employed to benefit from flow homogeneity, which greatly helps to improve the convergence of the results. Finally, probes are placed at various locations and record the primitive variables at every iteration.

Two averaging operators are needed when using the triple decomposition. Time-averaging is performed to obtain

the mean component of the flow and phase-averaging is employed to extract the mean and the coherent components together. The difference between the two therefore allows to isolate the coherent component. In this work, each period is decomposed into ten bins of equal width.

IV. Results

A. Baseline flow

To start with an overall description of the flow field, figure 1 shows instantaneous contours of density gradient magnitude at mid-span and streamwise velocity near the bump wall, at $y^+ \approx 10$. A fully turbulent boundary layer is observed upstream of the bump, with its characteristic streaks. Approaching the bump, the flow decelerates on the concave part and then quickly accelerates as it evolves on its convex part. The boundary layer undergoes partial re-laminarization due to the favorable pressure gradient there, which is also witnessed as the structures are widening in the spanwise direction. An oblique compression wave is generated when the flow separates and forms a large lambda pattern as it joins the normal shock standing downstream, responsible for the remaining compression. The separated shear layer is unstable, breaks down to turbulence and as a consequence, additional weak oblique compression waves are observed at the root of the normal shock. Finally, the boundary layer slowly recovers its initial, unperturbed state while reaching the end of the domain as thin and elongated structures appear again.

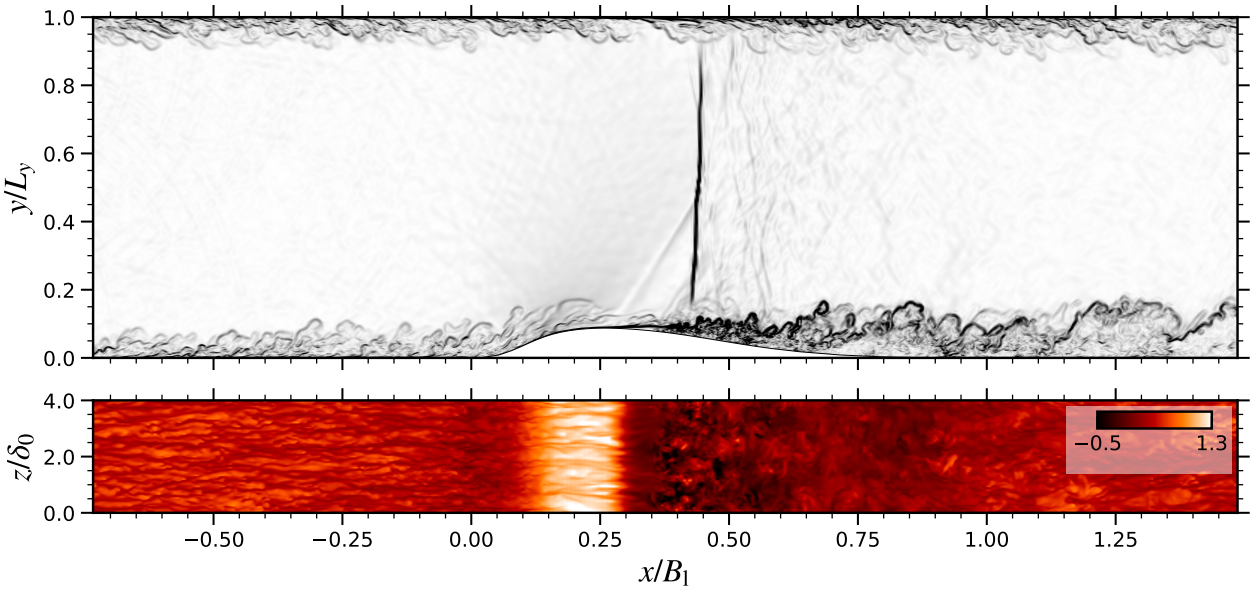

Fig. 1 Instantaneous density gradient magnitude at mid-span (*top*) and instantaneous streamwise velocity u/U_∞ near the bump wall, $y^+ \approx 10$ (*bottom*).

A sanity check of the computational setup is first performed, starting with an assessment of the grid resolution. Figure 2 shows the streamwise evolution of Δx^+, Δz^+ (assuming for both an equidistant distribution of the solution points) and the exact wall distance of the first solution point y^+_w, in wall units evaluated at the bottom wall. Upstream of

the bump, the resolution is close to the target values $\Delta x^+ = 16$, $\Delta z^+ = 12$ and $y_w^+ \approx 0.3$. The resolution remains around the target values or below, exception made of a short part of the bump over which it slightly worsens. At maximum, $\Delta x^+ \approx 30$, $\Delta z^+ \approx 20$ and $y_w^+ \approx 0.5$, which is still adequate for wall-resolved ILES.

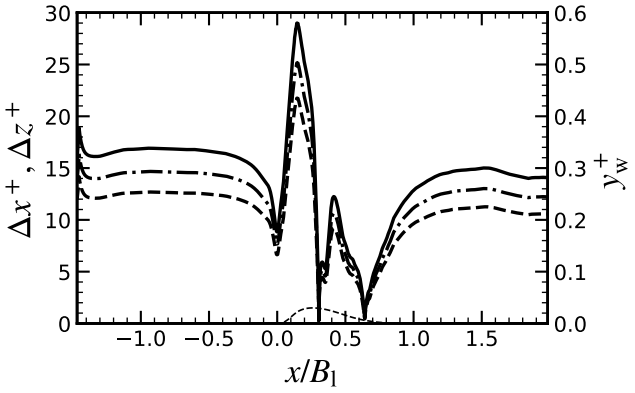

Fig. 2 Mesh resolution at the bump wall - Δx^+, Δz^+ and y_w^+, respectively, *solid*, *dashed* and *dashdot*. The *thin dashed* line represents the bump geometry.

The sanity check is pursued by looking at the quality of the boundary layer upstream of the bump. Figure 3 shows the mean velocity and Reynolds stress profiles in wall units, at the station $x/\delta_0 = -15$. The results are compared with DNS data for incompressible boundary layers [41] at the same Re_θ. The *dashed black* line indicates the Van Driest transformed velocity profile and is in perfect agreement with the incompressible normalization (*solid blue* line) in the viscous sub-layer and the logarithmic layer. However, a slight difference is observed in the defect layer, leading to a free stream velocity 1.4% lower with the incompressible normalization. The same agreement is found with respect to the DNS data but with a free stream velocity 1.9% lower. The Reynolds stresses show a very good fit. The overestimation of

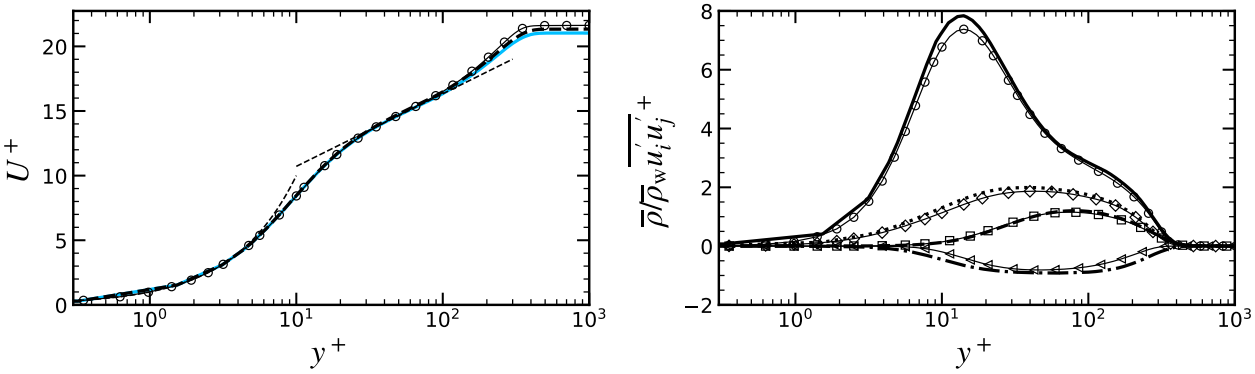

Fig. 3 Boundary layer profiles at $x/\delta_0 = -15$ - Streamwise velocity, incompressible (*solid blue*) and Van Driest normalization (*dashed black*) (*left*) and Reynolds stresses (*right*), with DNS data from Schlatter and Örlü [41] at $\mathrm{Re}_\theta = 1000$ (*symbols*).

the peak $\overline{u'u'}$ is an effect of the under-resolution [42]. These results show that the upstream boundary layer is properly developed and has recovered from the unrealistic treatment at the inlet plane, but also that compressibility effects are

small in this case. The latter was also highlighted by Wenzel et al. [43] by performing DNS of compressible turbulent boundary layers. The assumption of incompressibility is finally supported by considering the turbulence Mach number, defined by $\mathrm{M_t} = \overline{u_i' u_i'}^{1/2} / \overline{a}$. In the upstream boundary layer, it does not exceed 0.1, while it can reach 0.4 very locally on the downstream part of the bump. With the latter value, the difference between Favre and Reynolds averages for an adiabatic flat plate is of a few percents only [44].

Another aspect to check when simulating statistically two-dimensional turbulent flows is the spanwise extent of the domain, which should be sufficient to accommodate even the widest flow structures. Figure 4 shows the two-point streamwise velocity correlation coefficient in the spanwise direction at two stations, one upstream of the bump ($x/\delta_0 = -15$) and one downstream of the interaction ($x/\delta_0 = 16.67$). For both stations, the streamwise velocity is taken at a distance $y/\delta_0 = 0.5$ off the bottom wall. The correlation coefficient quickly drops to zero for the upstream station, at a distance $\Delta z/L_z \approx 0.08$. Downstream of the interaction, larger structures are expected because of the thickening of the boundary layer. The zero-crossing point of the correlation coefficient then lies at a further distance, $\Delta z/L_z \approx 0.25$. In any case, this occurs within half the domain width, which is therefore deemed to be sufficiently large.

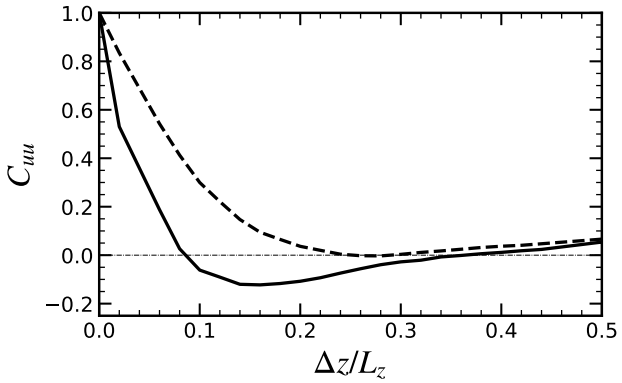

Fig. 4 Two-point streamwise velocity correlation coefficient in the spanwise direction at $y/\delta_0 = 0.5$ - stations $x/\delta_0 = -15$ (*solid*) and $x/\delta_0 = 16.67$ (*dashed*).

Figure 5 (*left*) depicts the mean friction coefficient. It first steadily decreases before getting influenced by the potential effect of the bump, further confirming that the inflow is far enough from the bump for the turbulence to develop properly. Over the bump, the friction coefficient reaches its maximum in the favorable pressure gradient region. The flow then separates slightly downstream of the section throat and reattaches on the downstream part of the bump. In between, the distribution is typical of thin separated zones [8] with first a short region over which the skin friction is barely negative, and a second, longer region with larger negative values. The superimposed PDF, shown only for the unperturbed case, further illustrates that the first part is associated with a low variance. It is actually referred to as the region of stable recirculation [12]. On very rare occasions, the flow almost reattaches. The second part exhibits a much higher variance that is linked to the vortex shedding occurring at the breakdown of the shear layer. A similar description can be found in previous studies on the same bump geometry, even though the flow conditions were different [10, 12] but

also for other configurations with [8] or without shock wave interaction [15, 17, 18]. Regarding the pressure coefficient on the bump wall (see figure 5, *right*), the upstream influence of the bump is observed too. The favorable pressure gradient region starts shortly downstream the beginning of the bump and extends up to the location of minimum C_p, right after the section throat. Downstream of the throat, pressure first rises as the flow undergoes compression from the weak oblique wave and reaches a plateau that corresponds to the region of stable recirculation. Further downstream, pressure rises again due to the effect of the normal shock and finally recovers to reach the imposed outlet value.

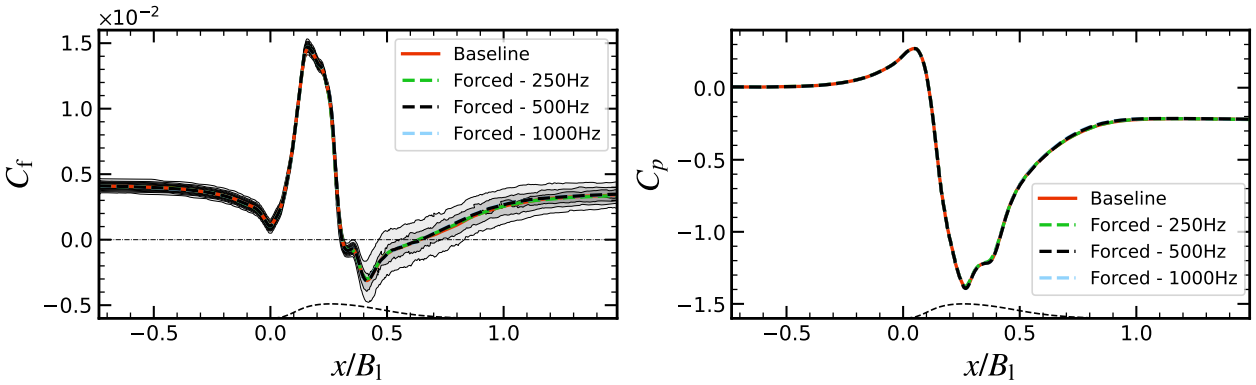

Fig. 5 Mean C_f with superimposed PDF from the unperturbed case, 8 equally-spaced contours between 0.02 and 0.40 (*left*), and mean C_p (*right*) on the bump wall. The *thin dashed* line represents the bump geometry.

The question whether the shock exhibits a large-scale motion is always of interest in shock wave/boundary layer interactions. For this purpose, the shock position has been monitored during the simulation. For each horizontal gridline, it is taken as the location of the maximum of pressure gradient magnitude. The mean shock position is illustrated in figure 6 (*left*) on averaged static pressure contours to show the range of height for which the shock detection is successful. The weighted pre-multiplied Power Spectral Density (PSD) map of shock motion, obtained from Fast Fourier Transform (FFT) and further normalized by its global maximum, is shown in figure 6 (*right*). This representation allows to emphasize the frequencies contributing the most to the variance of the signal. Dominant contributions are observed at $\mathrm{St}_{\delta_0} \approx 0.0077$ and $\mathrm{St}_{\delta_0} \approx 0.0135$ (200Hz and 350Hz, respectively). The emergence of two distinct low-frequency peaks is an artifact due to the relatively short simulation time with respect to those frequencies. Another, weaker, contribution is captured at $\mathrm{St}_{\delta_0} \approx 0.03$ (800Hz) near the edges. Especially, its influence starts to rise below $y/L_y \approx 0.3$, which correlates well with the weak compression waves.

To further comment on the major contributions to the shock motion, figure 7 shows their amplitude and their phase as a function of the height. The contributions at 200Hz and 350Hz exhibit a steadily increasing amplitude. For the higher frequency contribution at 800Hz, amplitude first decreases to reach a plateau from $y/L_y \approx 0.3$ to $y/L_y \approx 0.6$. Then, amplitude sharply rises. The evolution of phase indicates that the shock behaves differently below and above $y/L_y \approx 0.5$. All the contributions have a more or less constant phase in the lower part, meaning that the shock is moving as a whole. From $y/L_y \approx 0.5$, the phase first decreases to reach a minimum around $y/L_y \approx 0.75$ and then finally

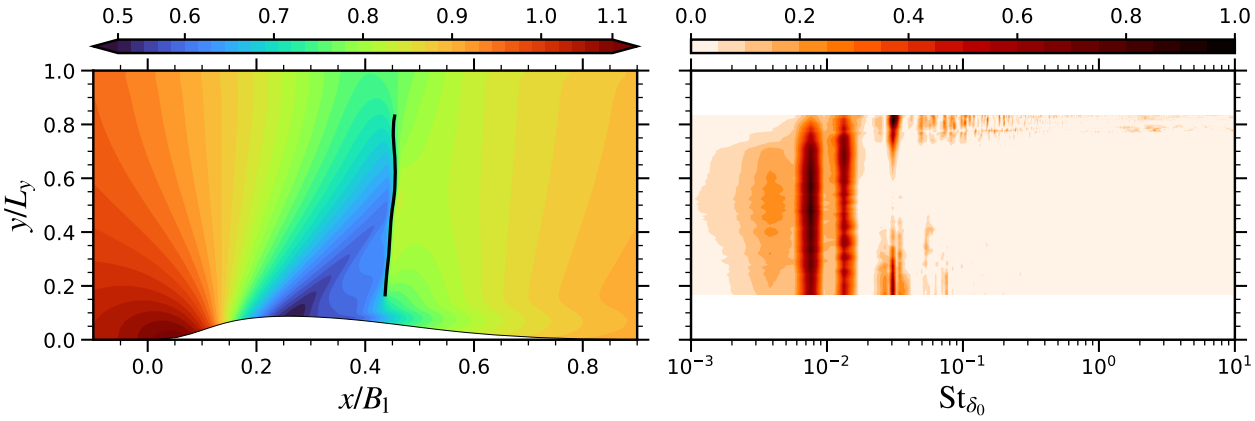

Fig. 6 Mean shock position superimposed on mean p/p_∞ contours (*left*) and weighted pre-multiplied PSD map of shock motion for the baseline case (*right*).

increases. This is more marked at 800Hz. The result is a global oscillatory motion of the shock. This different behavior is due to the oblique compression wave joining the normal shock at around mid-height, which brings additional stability through the mean flow gradients.

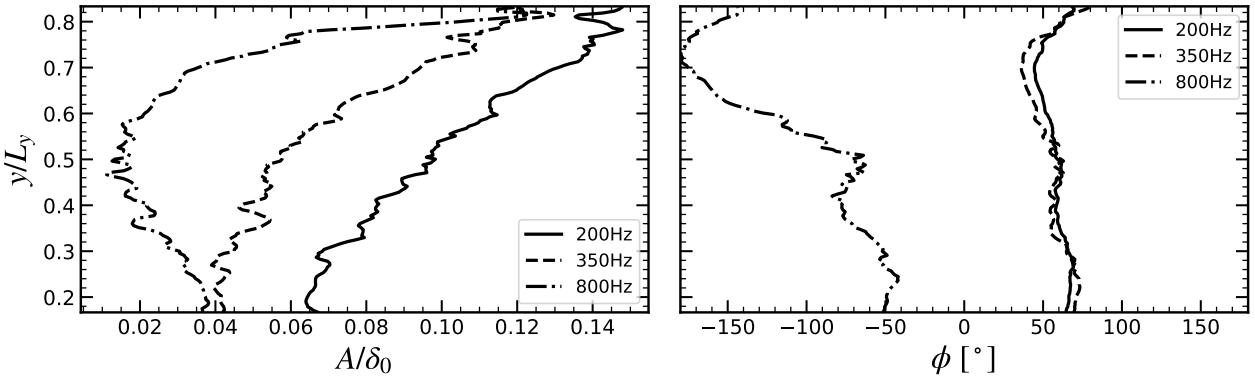

Fig. 7 Shock motion amplitude (*left*) and phase (*right*) of dominant contributions for the baseline case.

Figure 8 shows the weighted pre-multiplied PSD maps of static pressure at the bottom and top walls. The PSDs are evaluated using the Welch periodogram method [45] using 7 blocks and a 50% overlap, and are then normalized by the global maximum. Various locations are highlighted by *vertical* lines to ease the analysis. *Solid* lines refer to geometrical stations whereas *dashed* lines are related to physical phenomena. These locations are, from left to right, the beginning of the bump, the bump throat, the end of the region of stable recirculation, the reattachment point and the end of the bump.

The upstream boundary layer is characterized by a ridge centered at $\mathrm{St}_{\delta_0} \approx 1$. A broadband low-frequency energetic contribution is observed at both walls, around $\mathrm{St}_{\delta_0} = 0.01$. At the bottom wall, this contribution starts from the separation point and is consequently associated to the front leg of the lambda shock. It is moreover contained within the region of stable recirculation. At the top wall, this contribution is located at $x/B_1 \approx 0.45$, and it is therefore related to the normal shock (see figure 1). These results, together with the analysis made for figure 6, indicate that

the entire shock system is naturally oscillating. Actually, low-frequency unsteadiness at a Strouhal number that is two orders of magnitude lower than the incoming boundary layer is typical for shock wave/boundary layer interactions with separation [46]. At the bottom wall, the upstream ridge is progressively shifted toward $\mathrm{St}_{\delta_0} \approx 0.1$ in the interaction region. These intermediate frequencies develop as a consequence of the vortex shedding occurring at the breakdown of the shear layer, and persist in the downstream boundary layer from the reattachment point onward. Some contributions at intermediate frequencies are also captured at the top wall, downstream of the interaction, but most of the variance of the signal is due to the barely perturbed boundary layer.

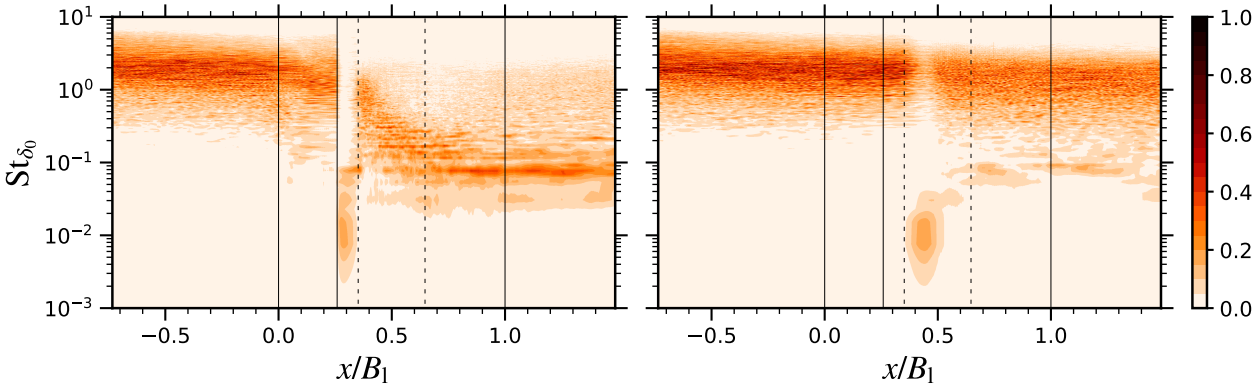

Fig. 8 Weighted pre-multiplied PSD maps of bottom (*left*) and top (*right*) wall pressure for the baseline case. The *vertical* lines indicate from left to right the beginning of the bump, the bump throat, the end of the region of stable recirculation, the reattachment point and the end of the bump.

Finally, time history of separation and reattachment point locations have been obtained, using span-averaged wall data. Not shown here but FFT reveals that the separation point mainly responds at 200Hz and 800Hz, whereas finding a dominant contribution for the reattachment point is much less obvious. The amplitude of the separation point motion ($\approx 0.055\delta_0$) is one order of magnitude lower than for the reattachment point. The latter lies indeed in a region which exhibits a high variance of friction coefficient as it has been described in figure 5.

B. Forced flow

To mimic the presence of rotor/stator interaction as in the blade passage of a turbomachine, the flow has been forced by imposing a sinusoidally fluctuating static pressure at the outlet boundary. To assess the effectiveness of the forcing, the FFT of the pressure signal acquired by a probe located at the center of the outlet cell, in the free stream ($y/L_y = 0.5$), is performed. In all cases, the deviation in amplitude is of a few percents at maximum and the second most energetic contribution represents less than 0.04% of the total energy content. It is therefore concluded that the forcing is effective.

Various flow features are now analyzed in order to highlight the effects of the forcing. First, a comparison of mean friction and pressure coefficients is provided in figure 5. No distinction can be made between the baseline and the three forced cases. It indicates first that the harmonic disturbance has no effect on these mean quantities, which is explained

by the low perturbation amplitude that has been prescribed. A marginal variation in the reattachment point location is observed when the flow is forced and could be attributed to the high variance in that region.

The response of the shock is assessed hereafter. In a similar manner as for the baseline case, figure 9 displays the weighted pre-multiplied PSD maps of the shock position. In all the cases, the forcing frequency clearly stands out at all heights as the main contributor to the variance of the signal. The influence of higher-order harmonics is slightly felt above $y/L_y \approx 0.65$. Furthermore, a modification of the behavior is observed for the lower part of the shock. For the 1000Hz case, a low-frequency contribution at $\mathrm{St}_{\delta_0} \approx 0.01$ comes at play, whereas nothing is highlighted for the lower perturbation frequency cases. It acts in the range $y/L_y \approx 0.2 - 0.6$, which corresponds rather well to the extent of the lambda shock. This low-frequency contribution was already pointed out for the natural motion of the shock. Its appearance at high forcing frequency could be explained by the diminished sensitivity of shock waves to high frequencies. A decoupling between the natural and the forced motions therefore occurs if the perturbation frequency increases. This would be in agreement with the limit case of an infinitely high forcing frequency, to which the shock would not be able to adapt and would therefore oscillate at its natural frequency.

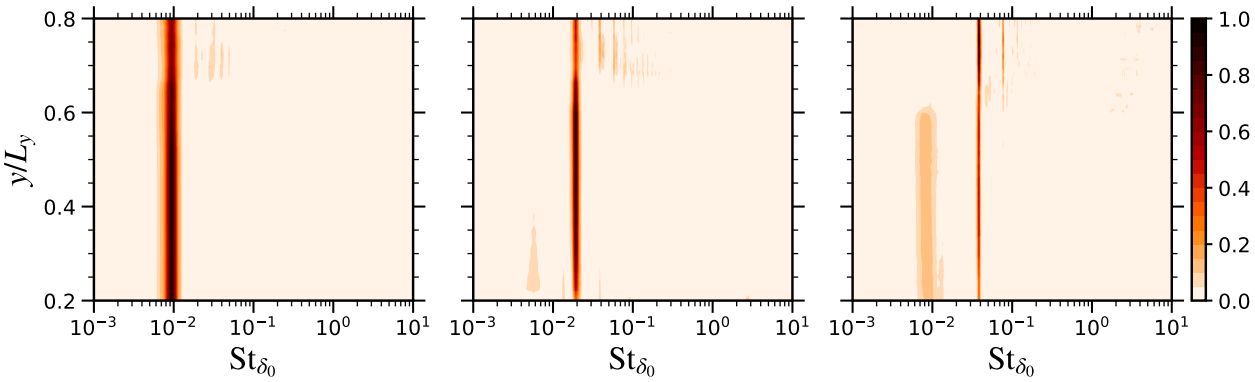

Fig. 9 Weighted pre-multiplied PSD maps of shock motion for the forced cases - 250Hz (*left*), 500Hz (*center*) and 1000Hz (*right*).

The amplitude and phase at the forcing frequencies as a function of height are depicted in figure 10. The evolution of amplitude occurs differently depending on the frequency. At 250Hz, amplitude first increases and reaches a plateau above $y/L_y \approx 0.6$. At higher frequencies, the amplitude grows almost monotonically. At 1000Hz, this growth is, however, very slow below $y/L_y \approx 0.6$ and the amplitude is of the same order of magnitude as for the baseline case. Globally, the amplitude is less at higher forcing frequency, which is an expected result [9, 47]. The inset on the *left* figure further illustrates the decrease of amplitude at $y/L_y = 0.4$ as a function of frequency. The evolution of phase confirms the change of dynamics above a certain height as it was demonstrated in the baseline case, except when the flow is forced at 250Hz. At that frequency, the shock system is much more disturbed and the upper part of the shock is actually vanishing during a short part of the oscillation period. The shock detection is then not successful and it is believed to be the cause of the discrepancy.

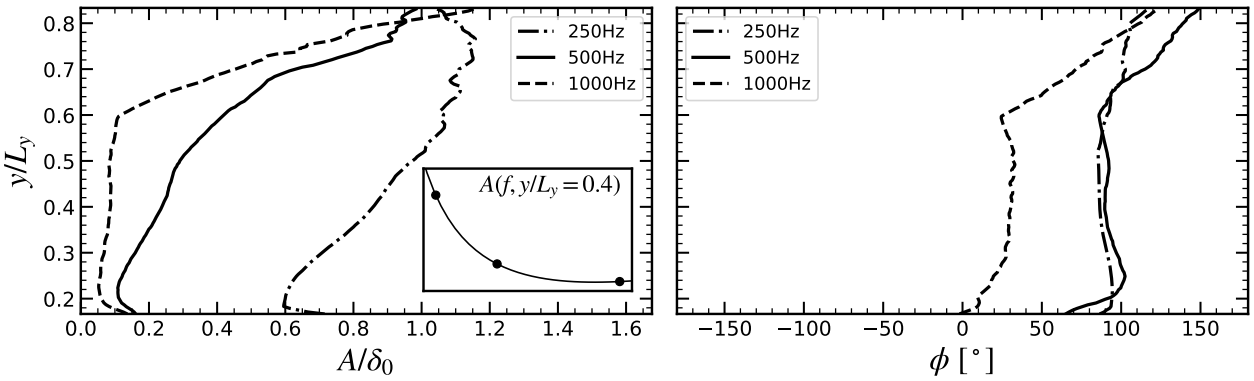

Fig. 10 Amplitude (*left*) and phase (*right*) of shock motion at the forcing frequencies for the forced cases.

Figure 11 shows the weighted pre-multiplied PSD maps of static pressure at the bottom and top walls, for each forced case. As for the baseline case, the PSDs are obtained by the Welch method, with $N_{\mathrm{bl}} = 9$ for the 250Hz and 500Hz cases, $N_{\mathrm{bl}} = 7$ for the 1000Hz case and a 50% overlap. When the flow is perturbed at 250Hz or 500Hz (respectively, *left* and *center* figures), strong influence of the forcing is evident right past flow separation at the bottom wall. In particular, the region of stable recirculation only receives a contribution corresponding to the forcing frequency. This influence persists further downstream and at some locations it conceals the contribution from the intermediate frequencies related to vortex shedding. At the top wall, the perturbation frequency is virtually the sole contributor in the region downstream of the interaction. The extent of the gap between the ridges corresponding to the upstream and downstream boundary layers (the latter being barely detectable) is larger at lower forcing frequency, and is directly reflecting the amplitude of the shock motion. When the flow is forced at 1000Hz (see *right* figures), the similarity with the baseline case is striking (see figure 8). At the bottom wall, the contribution from the forcing frequency is almost indistinguishable from the vortex shedding contribution. Approaching the separation bubble, its influence vanishes and the broadband low-frequency energetic region is retrieved at $\mathrm{St}_{\delta_0} \approx 0.01$, in the region of stable recirculation. At the top wall, the perturbation frequency stands out but the contribution from the natural shock oscillation is also detected.

The streamwise evolution of the bottom wall pressure amplification factor ($A_{\widetilde{P}_{\mathrm{w}}}/A_{\widetilde{P}_{\mathrm{o}}}$) at the forcing frequencies is illustrated in figure 12, *left*. For all the cases, the three first local extrema are co-located. The first and second amplification peaks are positioned at $x/B_{\mathrm{l}} \approx 0.3$ and $x/B_{\mathrm{l}} \approx 0.4$ and are caused by the oscillation of the weak oblique compression wave emanating from the separation point and of the normal shock, respectively. In between, the first attenuation peak is related to the end of the region of stable recirculation ($x/B_{\mathrm{l}} \approx 0.35$). Further downstream, in the subsonic boundary layer, a succession of lobes is observed. With increasing frequency, these lobes are shrunk and shifted toward more upstream locations, indicating upstream traveling waves. The ratio between the size of the first lobe (equal to half of the wavelength) and the period is constant for all frequencies and gives a propagation velocity of ≈ 87.5m/s. The frequency insensitivity of the pattern under the shock region compared to the downstream boundary

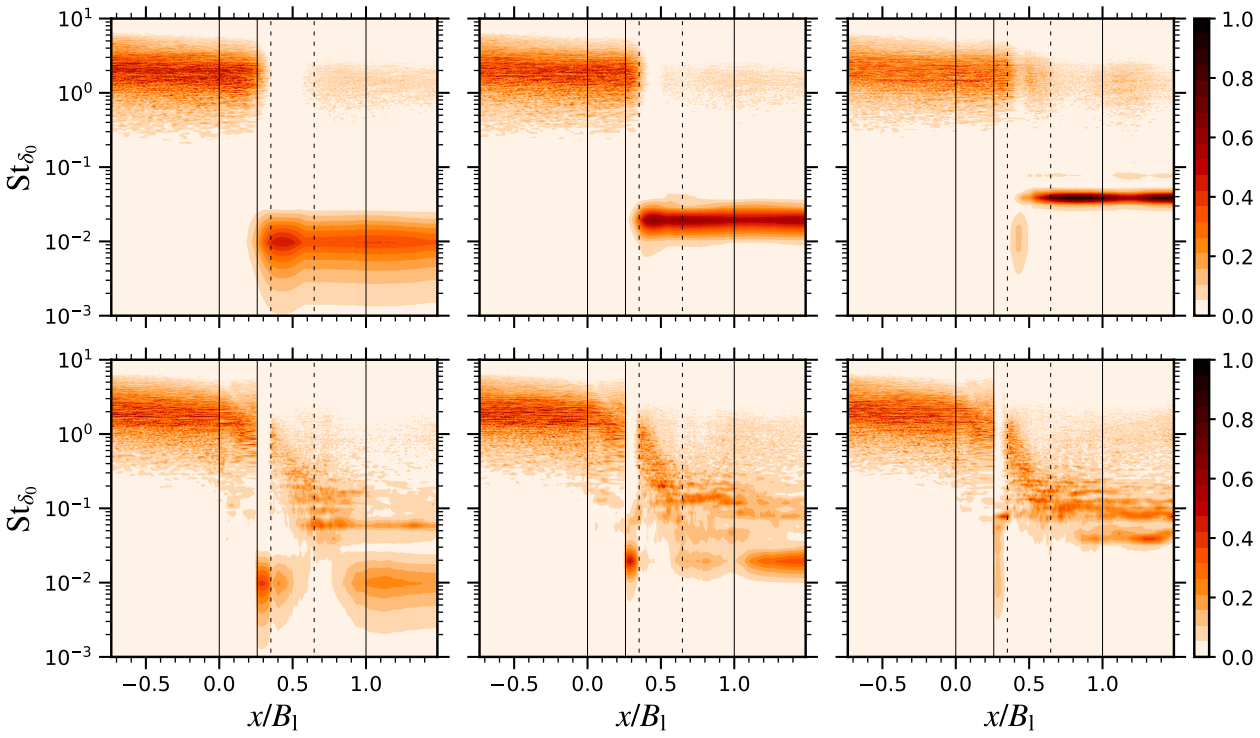

Fig. 11 Weighted pre-multiplied PSD maps of top (*top*) and bottom (*bottom*) wall pressure for the forced cases - 250Hz (*left*), 500Hz (*center*) and 1000Hz (*right*). The *vertical* lines are defined as in figure 8.

layer is in line with the conclusions of Bur et al. [19]. Acoustic waves are damped as they propagate upstream, because of viscous effects, and therefore the strong pressure amplification is due to the oscillation of the shock system in the region beneath. The shock system position being, on average, independent of the frequency, so are the locations of the three first extrema.

As a comparison, the results of URANS simulations are shown. The simulations are performed using Cadence FINE™/Turbo flow solver, initially developed by Rizzi et al. [48]. The trends predicted from the URANS corroborate qualitatively those provided by ILES. However, large discrepancies are noticed in terms of amplitude, and the first extrema are not correctly located, which can be explained as a shortcoming of URANS in resolving time-dependent phenomena. The available experimental results from Bron [9] at the reference Reynolds number are reported as well. Because of the different shock structure and separation bubble topology, no agreement is expected for the first extrema which are related to these features. Nonetheless, the first downstream lobe is reasonably well captured, revealing that the upstream propagation of pressure waves inside the boundary layer is not subject to Reynolds number effects. These comparisons give further confidence in the computational setup for the investigation performed in this work.

While the pattern beneath the shock region is independent of the frequency, the magnitude of the amplification factor is strongly affected and clearly decreases with increasing frequency. It actually reflects the extent of the shock system displacement. For a larger displacement (and therefore for a lower forcing frequency, see figure 10), a bigger

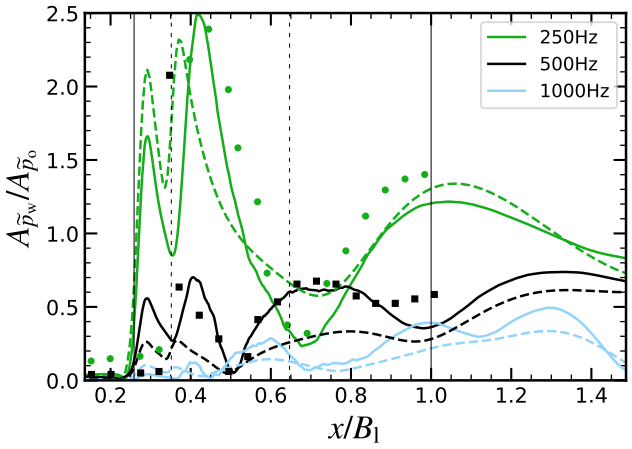

Fig. 12 Bottom wall pressure amplification factor - ILES (*solid*), URANS (*dashed*) and experiments from Bron [9] (*symbols*). The *vertical* lines are defined as in figure 8.

portion of the pressure gradient will be felt by a fixed point on the wall, resulting in a higher pressure amplitude.

Finally, but not illustrated here, the separation and reattachment points are mainly responding to the perturbation frequency when the flow is forced at 250Hz or 500Hz. At higher frequency, this influence is completely absent but the separation point shows a contribution from $\mathrm{St}_{\delta_0} \approx 0.01$, as in the unperturbed case. These observations are in line with the description of the wall pressure made from figure 11. Moreover, the amplitude of motion decreases with increasing frequency, similarly to the shock motion or the wall pressure amplitudes.

C. Coherent flow

1. Reference oscillator

Phase-averaging requires first the definition of a reference oscillator. For the 250Hz and 500Hz cases, a reference oscillator is obtained by reconstructing the signal of the separation point location with the sole contribution of the forcing frequency, its magnitude and phase being obtained from FFT of the original signal. The resulting reconstructed signals are illustrated in figure 13 on top of the original ones. The choice of the separation point location as a reference for these cases is justified first by the fact that the dominant contribution to that signal is at the forcing frequency. In addition, it seems more natural because the separation point is expected to be the point of formation of coherent structures, if they exist. This methodology does, however, not apply for the 1000Hz case since the separation point does not respond to the forcing. To allow a comparison, the prescribed outlet static pressure will be therefore used for that case. Using the outlet static pressure as a reference led to negligible changes in the results for the 250Hz and 500Hz cases, exception made of a shift in the bin number due to the phase difference between the two references. The computation of amplitude and phase is not affected by this change and these quantities can therefore be compared between the different cases.

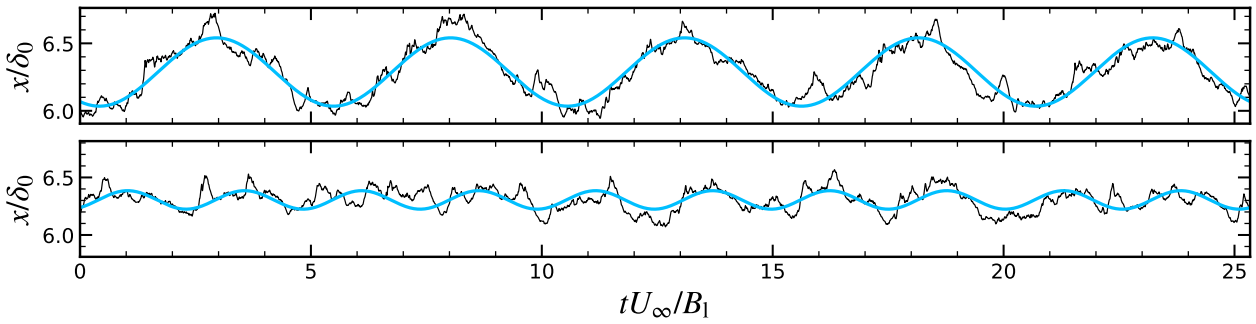

Fig. 13 Time evolution of separation point location (*thin black*) and reconstructed signal at the forcing frequency (*thick blue*) for the 250Hz (*top*) and 500Hz (*bottom*) cases.

2. Streamwise velocity

Figure 14 shows the time history of the coherent streamwise velocity (that is to say $\widetilde{u}$ for each bin arising from the phase average) for the 500Hz case. With respect to the reference oscillator, bin 2 corresponds to the most downstream position of the separation point, and bin 7 to its most upstream one. In the free stream, an upstream propagating wave is clearly discerned, which is the result of the forcing. This wave is of opposite sign compared to the pressure wave. The momentum equation in the streamwise direction for the coherent motion can be indeed simplified such that pressure forces balance convection, in the same way as for the mean flow. Starting from the separation point, a massive coherent structure develops in the line of the shear layer, and is further convected downstream as it changes of sign. When the separation point location is at the most downstream (bin 2), this structure exhibits highly positive values and changes sign as the separation point moves upstream. The weak oblique compression wave emanating from the separation point behaves in the same way.

Any coherent quantity $\widetilde{a}$ can be described by the amplitude and phase of the successive Fourier modes obtained by Fourier transform of the phase-averaged data. Figure 15 compares the amplitude and the phase of the first harmonic of $\widetilde{u}$ for the three forced cases. At the lowest frequency, a single structure is highlighted. It starts from the separation point, develops following the shear layer and then goes down to the bump wall further downstream. An analogous structure is also observed at 500Hz. With increasing frequency (or decreasing wavelength), the structure extent is smaller and the amplitude drops to zero at $x/B_1 \approx 0.75$. A second structure therefore shows up at $x/B_1 \approx 1.1$ which, at 250Hz, lies outside the figure. The amplitude is larger at lower frequencies. The maximum value of $\widetilde{u}/U_\infty$ at 500Hz is around 0.1, which corresponds to a large portion of the structure at 250Hz, as illustrated by the *dashed* contour. For the forced case at 1000Hz, coherent structures can be guessed at regularly-spaced intervals on the bump wall and in the shear layer, at $x/B_1 \approx 0.65$, $x/B_1 \approx 0.875$ and finally $x/B_1 \approx 1.1$, while no structure is found near the separation point. The convergence of the results is rather poor for this case, even though the data have been acquired over twenty periods. In contrast, convergence is good at 250Hz and 500Hz, with a lower number of periods. Because the downstream boundary layer is less sensitive to higher perturbation frequencies, the harmonic content at the forcing frequency diminishes as the

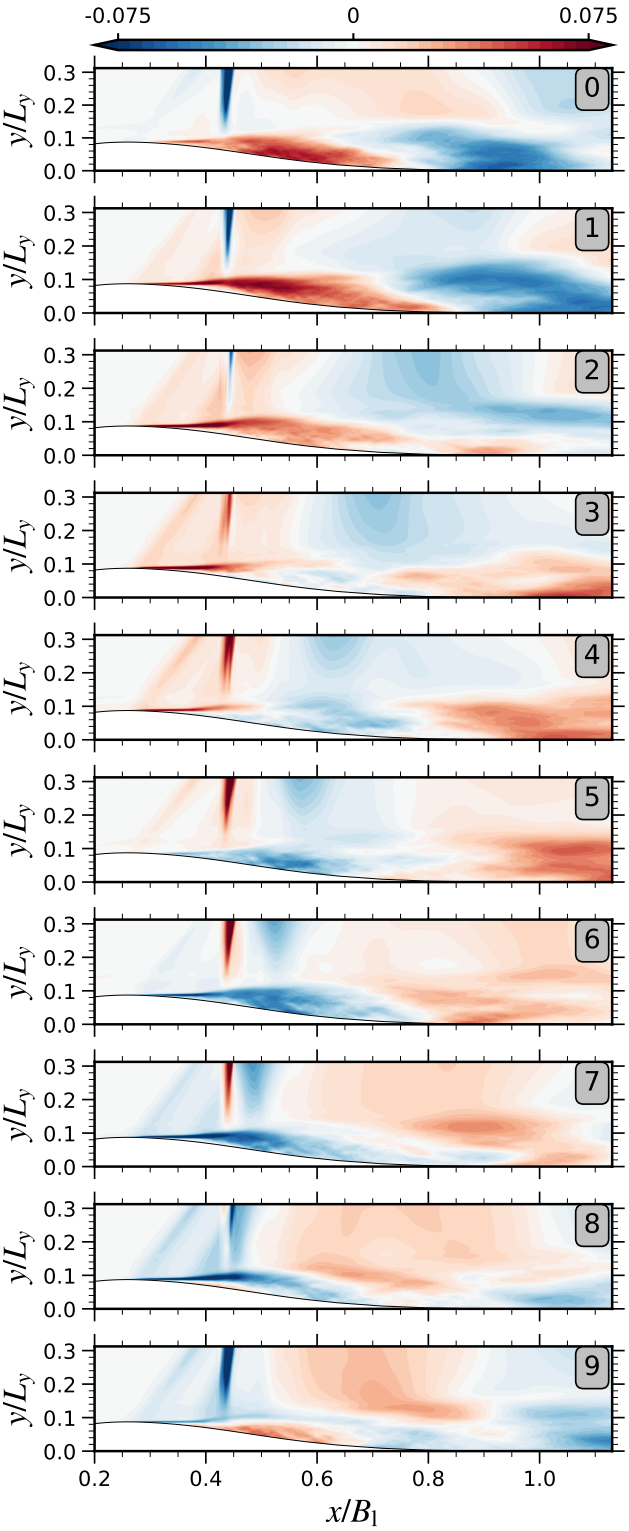

Fig. 14 Time history of $\widetilde{u}/U_\infty$ for the 500Hz case. The bin index is indicated in the top right corner of each subfigure.

forcing frequency increases. When the flow is perturbed at 1000Hz, the harmonic content is not significant enough and the phase average actually highlights non-converged statistics. The resemblance between the time history in figure 14 and the amplitude at 500Hz (figure 15, *center*) further demonstrates that the first mode corresponds to most of the harmonic energy content for that case. More than 90% of the total harmonic energy content is actually at the forcing frequency.

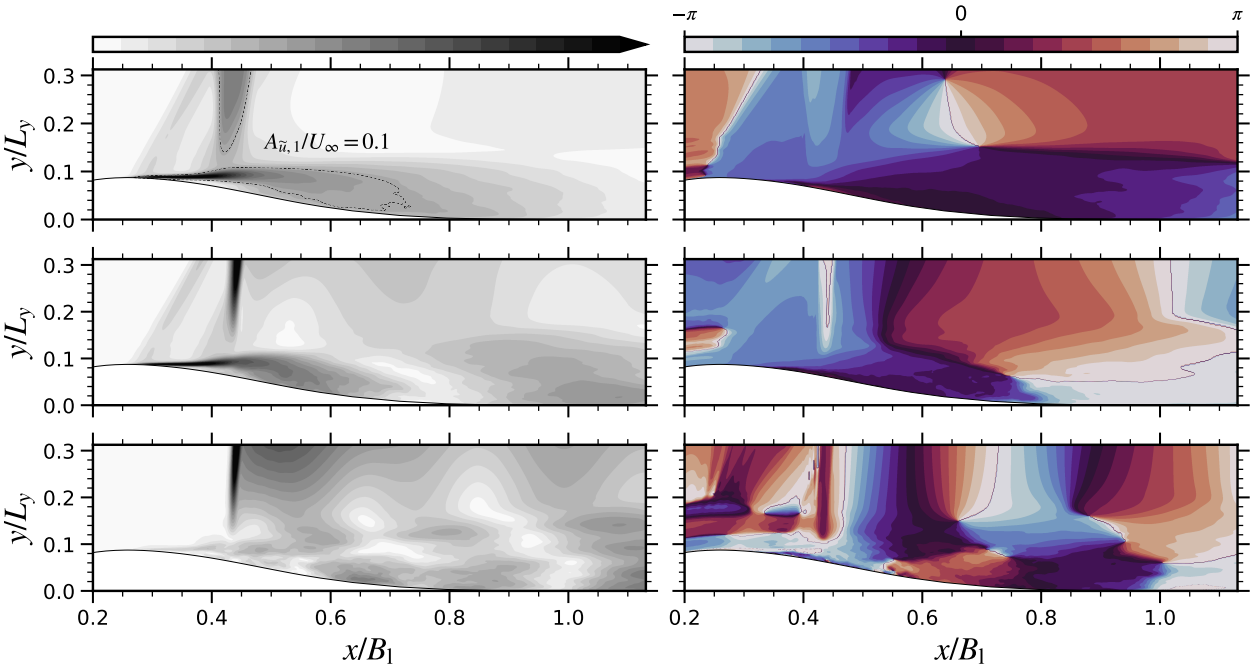

Fig. 15 Amplitude (*left*) and phase (*right*) of the first harmonic of $\widetilde{u}/U_\infty$ - 250Hz (*top*), 500Hz (*center*) and 1000Hz (*bottom*). Amplitude is bounded between 0 and, respectively, 0.3, 0.1 and 0.05.

3. Turbulence kinetic energy

In a similar manner, figure 16 compares the amplitude and the phase of the first harmonic of turbulence kinetic energy, for the three forced cases. Focusing first on the 250Hz case, various structures are easily noticed. Starting from the separation point, two layers are discerned. The outer layer consists of a single, elongated and strong structure, following the shear layer, whereas below, the inner layer develops as several, smaller and weaker structures, located at $x/B_1 \approx 0.33$, $x/B_1 \approx 0.38$ and $x/B_1 \approx 0.46$. The first of these is actually better seen on the phase. The phase moreover indicates that these inner layer structures are of alternating signs, the second being in phase with the outer layer structure. At 500Hz, this two-layers pattern is also discernible. Interestingly, the cores of those structures are co-located with the ones described at 250Hz, reminding the frequency insensitivity of the wall pressure amplification factor pattern beneath the shock system. The outer layer structure and the third inner layer structure are nevertheless shrunk because of the reduced wavelength. As a consequence, an additional structure is found in the shear layer downstream (at $x/B_1 \approx 0.9$). At 1000Hz, convergence is poorer. The shear layer shows, however, a succession of structures which recalls the ones

highlighted for the streamwise velocity.

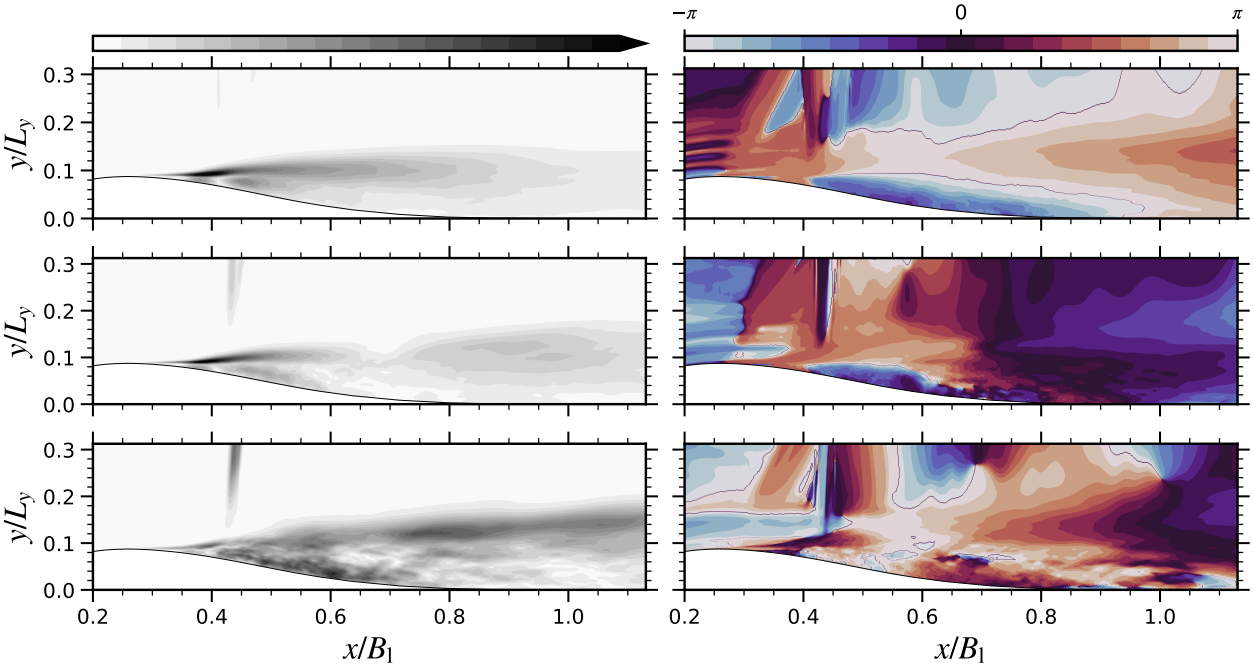

Fig. 16 Amplitude (*left*) and phase (*right*) of the first harmonic of $\widetilde{k}/U_\infty^2$ - 250Hz (*top*), 500Hz (*center*) and 1000Hz (*bottom*). Amplitude is bounded between 0 and, respectively, 0.05, 0.02 and 0.005.

Once again, the amplitude of the modulation is seen to increase as the frequency decreases, and the coherent turbulence kinetic energy is actually not negligible. At some stations, $\widetilde{k}/\overline{k}$ can amount to about 60% at 250Hz and to about 20% at 500Hz, when comparing the maximum values. Comparing the local values, these ratios can be even higher. Indeed, because of the periodic forcing, mean and harmonic components of turbulence kinetic energy do not necessarily peak at the same distance off the wall.

4. Turbulent stress budgets

The budgets of the different turbulent stresses are presented here for the 500Hz case first. Figure 17 depicts the budgets of the mean turbulence kinetic energy $\overline{k}$ and the mean turbulent normal stresses $\overline{u'u'}$, $\overline{v'v'}$ and $\overline{w'w'}$. Two stations are defined such that they cross the cores of the first coherent structures. The left column refers to the station $x/B_l = 0.33$ and the right one to $x/B_l = 0.38$. The budgets are shown as a function of the distance from the bump wall (d^+, in upstream wall units).

At the first station, the budget of $\overline{k}$ is dictated only by $\overline{u'u'}$ since the terms for the other normal stresses are two orders of magnitude lower. The main area of activity is the shear layer. Production is the dominant source term and peaks at $d^+ \approx 34$. The corresponding sink terms are convection, with the side contributions of dissipation, viscous diffusion and turbulent diffusion. Only pressure diffusion is inactive. Regarding $\overline{v'v'}$, pressure strain and pressure diffusion are balancing each other from the wall up to the mixing layer. Further away from the wall, previously inactive

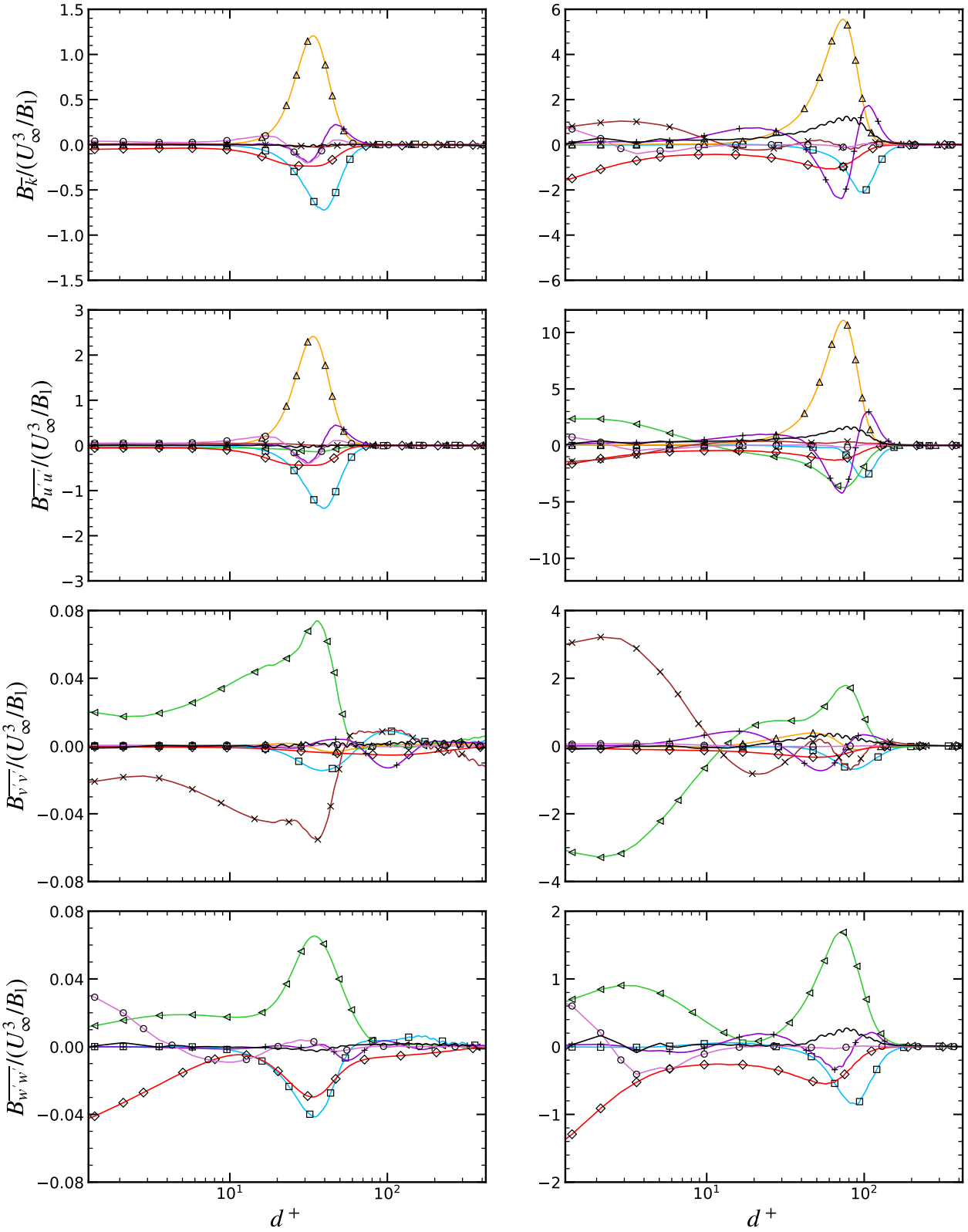

Fig. 17 **Budgets of $\overline{k}$, $\overline{u'u'}$, $\overline{v'v'}$ and $\overline{w'w'}$ at $x/B_l = 0.33$ (*left*) and $x/B_l = 0.38$ (*right*) for the 500Hz case - Convection (□), production (△), pressure strain (◁), dissipation (◇), viscous diffusion (○), pressure diffusion (×), turbulent diffusion (+) and balance (*solid black*).**

terms such as advection and turbulent diffusion come at play, whereas pressure strain drops to zero. Finally, the budget of $\overline{w'w'}$ shows two areas of activity. In the near-wall region, pressure strain, dissipation and viscous diffusion are the only actors, whereas in the shear layer, viscous diffusion vanishes and convection comes to prominence. Last but not least, pressure strain is a sink term for $\overline{u'u'}$ (even though barely apparent) and redistributes the energy to $\overline{v'v'}$ and $\overline{w'w'}$, where it appears as a source term. It therefore plays the same role as typically observed in attached boundary layers [49].

Further downstream, at the second station, the behavior is modified regarding different points. First, the redistribution of energy due to the pressure strain term occurs differently. In the near-wall region, energy is transferred from $\overline{v'v'}$ to $\overline{u'u'}$ and $\overline{w'w'}$. In the mixing layer, the classical behavior is recovered, where $\overline{u'u'}$ acts as the only provider for the other normal stresses. Moreover, terms from $\overline{v'v'}$ and $\overline{w'w'}$ play now a role in the budget of $\overline{k}$. In particular, near-wall dissipation comes equally from $\overline{u'u'}$ and $\overline{w'w'}$ and pressure diffusion from $\overline{u'u'}$ and $\overline{v'v'}$. Finally, a second area of activity appears near the wall for $\overline{u'u'}$, which is also affecting the budget of $\overline{k}$. Production is, however, again the dominant term by far and peaks further away from the wall, at $d^+ \approx 74$, following the development of the shear layer. The maximum peak is actually located slightly more downstream, at the minimum of friction coefficient ($x/B_\mathrm{l} \approx 0.4$), and rises to 6.2 (normalized by U_∞^3/B_l).

The budget of $\overline{k}$ was also reported in Marquillie et al. [14], Laval and Marquillie [15], Schiavo et al. [18] on a bump without shock wave interaction, at the location of minimum C_f. Although the configurations are different, a very good agreement is noted with respect to the second station here, which is indeed very close to the minimum C_f, at $x/B_\mathrm{l} \approx 0.41$ (see figure 5). Of particular interest is the three-peaks distribution of turbulent diffusion, showing two positive peaks (and therefore a gain of energy) around the production peak and acting as the main sink term (a negative peak) where production is at its maximum. This was also highlighted experimentally in boundary layers subjected to strong adverse pressure gradients [50]. Finally, the near-wall equilibrium between pressure strain and pressure diffusion in the budget of $\overline{v'v'}$ was also reported in Vyas et al. [51] for an oblique shock wave/boundary layer interaction.

The budget of $-\overline{u'v'}$ is shown in figure 18 at the same two locations. The first station depicts mainly two contributors, that is to say pressure strain and pressure diffusion, balancing each other regardless of the distance from the wall. Smaller contributions of convection and production are seen in the mixing layer. At the second station, terms involving pressure are still present and balance each other almost perfectly. Again, this was documented in Vyas et al. [51]. Furthermore, in the shear layer, production is now taking the lead and turbulent diffusion, up to now benign, becomes active in this region. It exhibits a similar threefold pattern as in the budget of $\overline{k}$, with one peak counterbalancing the maximum of production and two surrounding peaks of opposite sign.

The sum of all terms (or the balance) is equivalent to the temporal derivative in the turbulent stress equations and should in principle be zero for the mean stresses. This is verified at $x/B_\mathrm{l} = 0.33$ but it is not necessarily the case at $x/B_\mathrm{l} = 0.38$. The same unbalance was noted in Schiavo et al. [17, 18] for an incompressible flow over a bump, with a similar grid resolution ($\Delta x^+ \approx 16 - 21$, $y_\mathrm{w}^+ \approx 0.11 - 0.17$ and $\Delta z^+ \approx 15 - 21$). Consequently, it is an effect of the

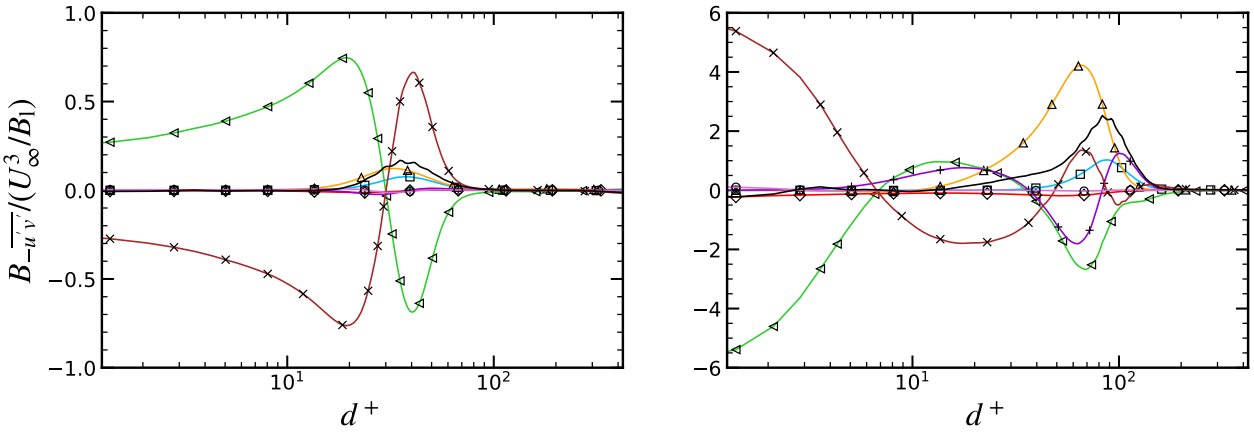

Fig. 18 Budgets of $-\overline{u'v'}$ at $x/B_1 = 0.33$ (*left*) and $x/B_1 = 0.38$ (*right*) for the 500Hz case. Symbols are defined as in figure 17.

mesh, and not of the neglected compressibility effects. The mesh is slightly under-resolved and dissipation is therefore under-estimated at the second station.

To close the analysis of the mean budgets, the additional convection and production terms arising from the triple decomposition (see equations 6 and 7a) were found to be two orders of magnitude smaller and, as a consequence, are negligible. This constitutes another proof that the forcing has no effect on the mean flow and, more specifically here, on the mean turbulent stresses. The budgets in the baseline case were checked and are identical. They are, however, not shown here for the sake of brevity. Consequently, the distribution of mean turbulent stresses is the same whether the flow is forced or not.

Coherent turbulent stresses budgets have also been computed from the data. Figure 19 illustrates the budgets of $\widetilde{k}$, $\widetilde{u'u'}$, $\widetilde{v'v'}$ and $\widetilde{w'w'}$ at the two stations defined previously. The results are shown only for bin 2, corresponding to the most downstream location of the separation point, and for the case at 500Hz.

At the first station, the budget of $\widetilde{k}$ is controlled by $\widetilde{u'u'}$, as terms involved in the other normal stresses budgets are one order of magnitude lower. For $\widetilde{u'u'}$, production is again the most dominant contribution with two peaks of opposite sign (the maximum being located at $d^+ \approx 25$ and the minimum at $d^+ \approx 42$), instead of a single peak. The modulation accounts for around 25% of the local mean production. In between, coherent production is null at the distance from the wall at which the mean production is maximum (see figure 17). Most of the production is either transported as the convection term is of importance or diffused by viscous or turbulent effects. Turbulent diffusion shows four peaks of alternating signs, which can actually be seen as two overlapping three-peaks distributions, one around each production extremum. Finally, dissipation and pressure strain give modest contributions. In the case of $\widetilde{v'v'}$, terms involving pressure are found to be prominent. Finally, the budget of $\widetilde{w'w'}$ is commanded by dissipation, pressure strain and viscous diffusion at the wall. Further away from the wall, convection and pressure strain are the active terms.

Moving to the second station, two areas of activity are discerned. In the near-wall region, the budget of $\widetilde{k}$ is

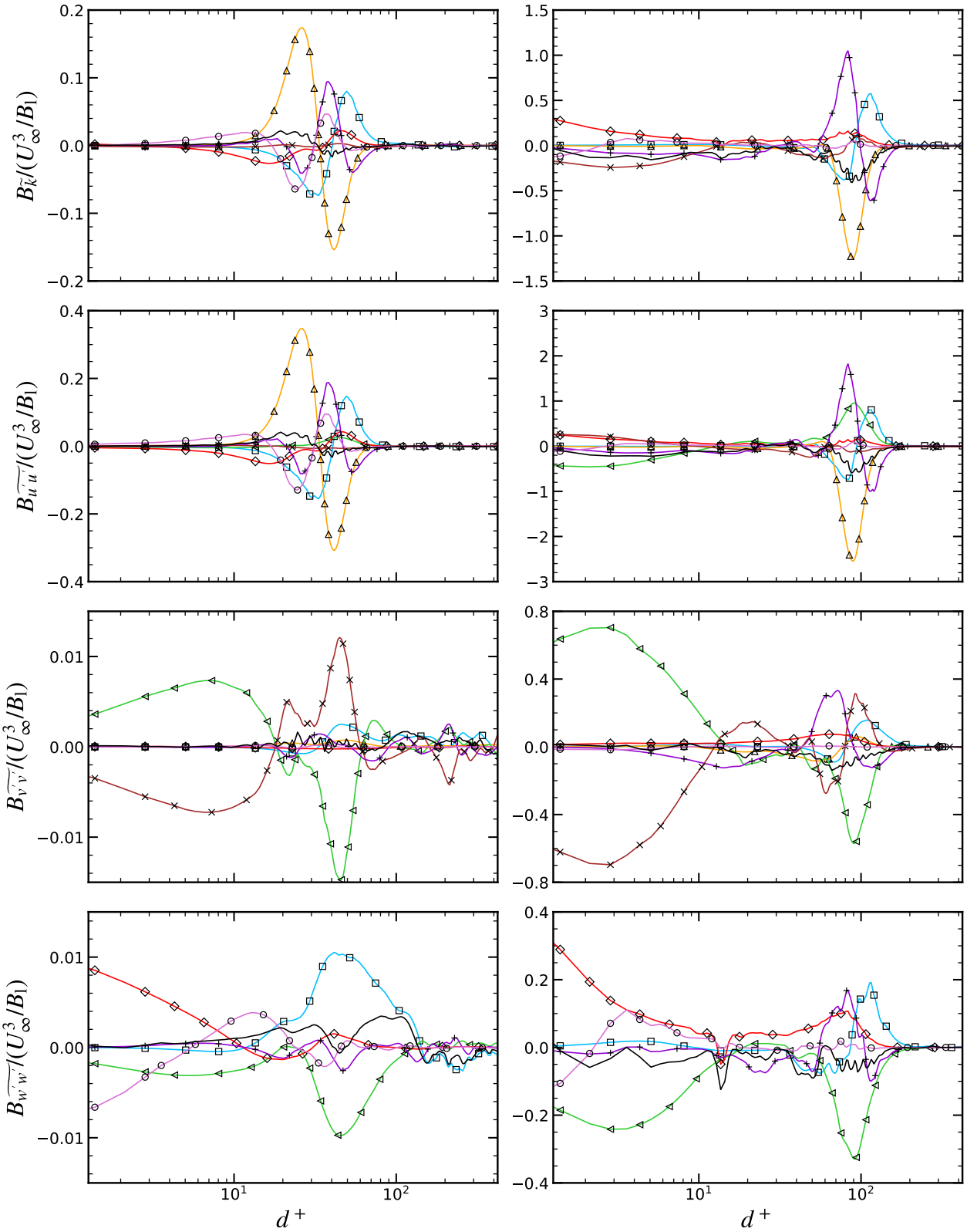

Fig. 19 **Budgets of $\widetilde{k}$, $\widetilde{u'u'}$, $\widetilde{v'v'}$ and $\widetilde{w'w'}$ for bin 2 at $x/B_l = 0.33$ (*left*) and $x/B_l = 0.38$ (*right*) for the 500Hz case. Symbols are defined as in figure 17.**

dominated by dissipation, pressure diffusion and viscous diffusion. The former comes from $\widetilde{u'u'}$ but also, and more importantly, from $\widetilde{w'w'}$. Pressure diffusion finds its origin in the budget of $\widetilde{v'v'}$. The second area is the shear layer. Production displays this time a single peak, coming only from $\widetilde{u'u'}$ and located slightly further away from the wall compared to the location of the mean peak production ($d^+ \approx 84$ for the coherent against $d^+ \approx 74$ for the mean). Compared to the first station, viscous diffusion is absent for the benefit of turbulent transport and convection. Turbulent diffusion shows again a three-peaks pattern. The peak modulation of turbulent diffusion is very high and reaches nearly 50% of the local mean value.

The budgets of $-\widetilde{u'v'}$ are depicted in figure 20 for the two same stations. At the first station, pressure strain and pressure diffusion are the main contributions and cancel each other almost perfectly. The nodes correspond to the anti-nodes of the same contributions in the mean budget. Further downstream, terms involving pressure balance each other in the near-wall region. Away from the wall, production and turbulent diffusion become major contributors as well. Production shows again a single peak, co-located with the positive peak of turbulent diffusion at $d^+ \approx 78$. As for the mean budgets, two other peaks of turbulent diffusion are surrounding the production peak.

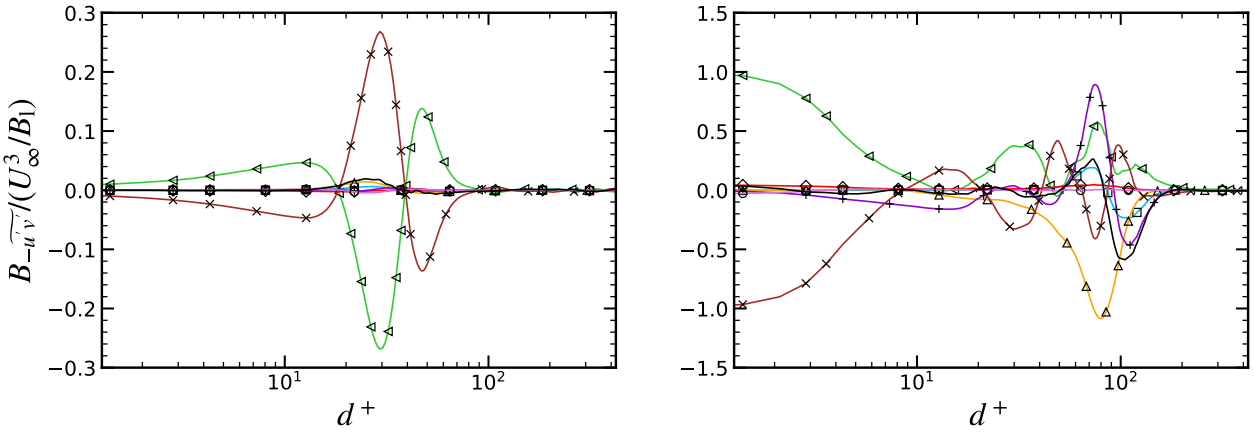

Fig. 20 Budgets of $-\widetilde{u'v'}$ for bin 2 at $x/B_l = 0.33$ (*left*) and $x/B_l = 0.38$ (*right*) for the 500Hz case. Symbols are defined as in figure 17.

The results are provided here for the forced case at 500Hz. The mean budgets were found to be independent of the forcing frequency, in agreement with previous observations. The coherent budgets at 250Hz show the same distributions (not illustrated here for the sake of brevity) at $x/B_l = 0.33$ and $x/B_l = 0.38$, but the modulation is stronger. For example, the production peaks of $\widetilde{u'u'}$ and $\widetilde{u'v'}$ at $x/B_l = 0.38$ are both 2.5 times higher. At 1000Hz, nothing comparable could be highlighted and the modulation is low.

5. Turbulence production

As in simple shear flows, the noticeable production terms originate from the shear, which is the most significant velocity gradient. For the mean production, these are due to the mean shear and the dominant contributions are

$-2\overline{u'v'}\partial\overline{u}/\partial y$ and $-\overline{v'v'}\partial\overline{u}/\partial y$ for $\overline{u'u'}$ and $\overline{u'v'}$, respectively. The production of $\widetilde{u'u'}$ is caused by the mean shear and its modulation, and mainly comes from two terms (out of eight), $-2\overline{u'v'}\partial\widetilde{u}/\partial y$ and $-2\widetilde{u'v'}\partial\overline{u}/\partial y$. They are representing, respectively, the action of the coherent flow upon the mean component of the shear stress and the action of the mean flow upon the coherent component of the shear stress. These terms are compared all together in figure 21 for the two stations $x/B_l = 0.33$ and $x/B_l = 0.38$. The sum of the two dominant terms alone is also represented in *dashed blue* to allow a direct comparison with the total production, in *solid black*. Whereas the agreement is very good for the second station, some information is missing at the first station if one wants to recover the total production more accurately. Taking into account the contributions from compressive/extensive strain, namely $-2\overline{u'u'}\partial\widetilde{u}/\partial x$ and $-2\widetilde{u'u'}\partial\overline{u}/\partial x$, helps in that direction. Nevertheless, they remain one order of magnitude lower. Even though these results have been obtained in a separated flow, they are in agreement with experimental observations on attached turbulent boundary layers subjected to oscillatory shear [24]. Regarding production of $-\widetilde{u'v'}$, two contributions (out of sixteen) are found to be dominant. These are $\overline{v'v'}\partial\widetilde{u}/\partial y$ and $\widetilde{v'v'}\partial\overline{u}/\partial y$.

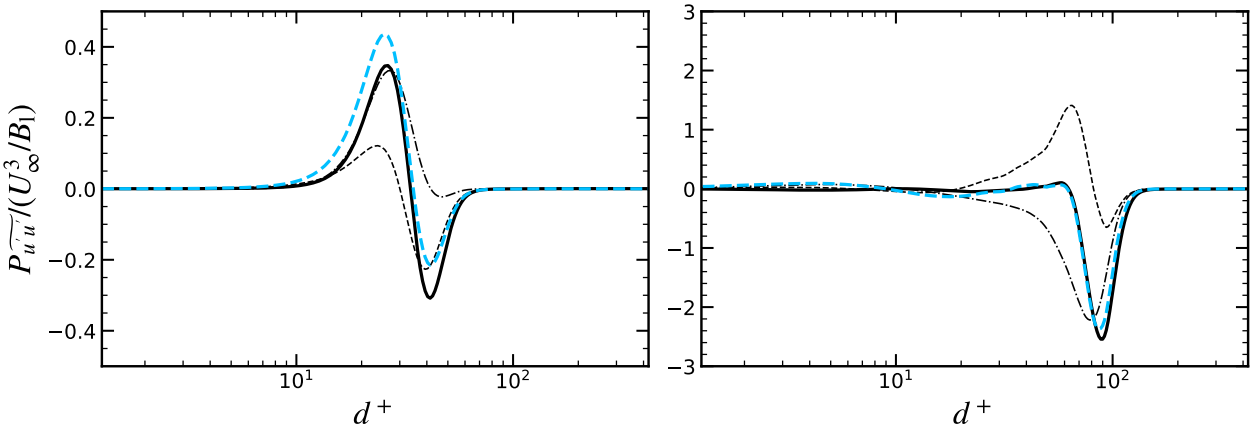

Fig. 21 Coherent production of $\widetilde{u'u'}$ for bin 2 at $x/B_l = 0.33$ (*left*) and $x/B_l = 0.38$ (*right*) for the 500Hz case - Total production (*solid*), $-2\overline{u'v'}\partial\widetilde{u}/\partial y$ (*dashed*), $-2\widetilde{u'v'}\partial\overline{u}/\partial y$ (*dashdot*), $-2\overline{u'v'}\partial\widetilde{u}/\partial y - 2\widetilde{u'v'}\partial\overline{u}/\partial y$ (*dashed blue*).

The fact that only these two contributions are sufficient to represent the production is an important finding regarding turbulence modeling in the NLH method. Considering an eddy viscosity model, the coherent turbulent stress can be written as the sum of two terms,

$$\widetilde{u_i'u_j'} = -\overline{\nu}_T\widetilde{s}_{ij} - \widetilde{\nu}_T\overline{s}_{ij} \tag{12}$$

where $\overline{\nu}_T$ is the eddy viscosity evaluated with the mean flow while $\widetilde{\nu}_T$ accounts for the effect of the harmonic flow. Since the strain-rate tensor reduces to $\partial u/\partial y$, the two dominant production terms can actually be associated to the two terms modeling the coherent turbulent stresses. For forced flows involving a massive separation, both contributions were shown to be essential when using frequency-domain approaches [4]. The present results demonstrate the ability of the methodology employed to capture the two effects and therefore the data generated to be used to improve harmonic

turbulence models.

V. Conclusion

Wall-resolved implicit large-eddy simulations of the transonic flow over a bump have been performed performed. The flow conditions are chosen to reproduce features encountered in transonic turbomachines: a shock wave develops in the passage and interacts with the boundary layer, and the potential effect of a rotor/stator interaction is accounted for by imposing a back pressure that is fluctuating in time periodically. Various realistic forcing frequencies are investigated.

The unperturbed case highlights a large lambda shock system with a massive flow separation on the downstream part of the bump. The shock system is found to oscillate naturally at a frequency corresponding to $\mathrm{St}_{\delta_0} \approx 0.01$.

When the flow is subjected to a periodic forcing, no difference is observed between the mean unperturbed and the mean perturbed solutions. However, unsteady aspects are considerably modified and the sensitivity of the flow is shown to be higher for lower forcing frequencies. At 250Hz and 500Hz, the baseline behavior is completely obscured and the entire flow responds mainly to the perturbation. At the highest frequency (1000Hz), the influence of the forcing diminishes. In particular, the separation bubble acts as in the baseline case and a decoupling between the natural and the forced shock oscillation is observed.

A complex pattern of wall pressure amplification factor is pointed out and reveals a twofold response of the downstream boundary layer. The three first extremum locations - beneath the shock region - are independent of the frequency. Their amplitude is nevertheless related to the sensitivity of the shock system to the forcing. Downstream lobes are linked to the upstream propagating pressure wave and their spatial extent is ruled by the wavelength of the signal. These lobes are moreover damped as the wave is traveling upstream.

To extract the harmonic component of the flow, phase-averaging has been carried out using a reference oscillator based on the separation point. Because of the higher sensitivity of the flow at low frequency, this is especially successful for the 250Hz and 500Hz cases. Coherent structures of streamwise velocity and turbulence kinetic energy are emphasized. Their layout is independent of the frequency in the region of influence of the shock system. More specifically, coherent turbulence kinetic energy is organized in a two-layers pattern starting from the separation point, with a single and strong outer-layer structure following the development of the shear layer and an inner-layer comprising smaller structures with alternating sign.

Mean and coherent turbulent stress budgets have been obtained and are analyzed at various stations. Convection, production and turbulent diffusion stand out as the major contributors to the budget of turbulence kinetic energy whereas pressure strain and pressure diffusion are prominent in the shear stress budget. A typical pattern of mean turbulent diffusion for boundary layers in adverse pressure gradient is reproduced, that is to say a three-peaks distribution around the production peak. Results show that this can be extended to the coherent turbulent transport regardless of the number of coherent production peaks.

The decomposition of the coherent production terms allows to isolate only two dominant contributions, coming from the mean and harmonic shears. It further confirms the necessity of considering a mean and a harmonic eddy viscosity when simulating massively separated flow using frequency-domain approaches. The current methodology is able to capture both effects and, as a future step, the database generated will serve to improve coherent turbulent stress modeling in that framework.

Acknowledgement

This work is part of a project that has received funding from the European Union's Horizon 2020 research and innovation programme under grant agreement No 860909 (TEAMAero - Towards Effective Flow Control and Mitigation of Shock Effects In Aeronautical Applications).

References

[1] He, L., and Ning, W., "Efficient Approach for Analysis of Unsteady Viscous Flows in Turbomachines," *AIAA Journal*, Vol. 36, No. 11, 1998, pp. 2005–2012. https://doi.org/10.2514/2.328.

[2] Vilmin, S., Lorrain, E., Hirsch, C., and Swoboda, M., "Unsteady Flow Modeling Across the Rotor/Stator Interface Using the Nonlinear Harmonic Method," *Turbo Expo: Power for Land, Sea, and Air*, Vol. 4241, 2006, pp. 1227–1237. https://doi.org/10.1115/GT2006-90210.

[3] Hall, K. C., Thomas, J. P., and Clark, W. S., "Computation of Unsteady Nonlinear Flows in Cascades Using a Harmonic Balance Technique," *AIAA Journal*, Vol. 40, No. 5, 2002, pp. 879–886. https://doi.org/10.2514/2.1754.

[4] Philit, M., Ferrand, P., Labit, S., Chassaing, J., Aubert, S., and Fransson, T., "Derivated Turbulence Model to Predict Harmonic Loads in Transonic Separated Flows over a Bump," *28th International Congress of Aeronautical Sciences*, 2012. URL https://www.icas.org/ICAS_ARCHIVE/ICAS2012/PAPERS/773.pdf.

[5] Tucker, P., "Computation of Unsteady Turbomachinery Flows: Part 1—Progress and Challenges," *Progress in Aerospace Sciences*, Vol. 47, No. 7, 2011, pp. 522–545. https://doi.org/10.1016/j.paerosci.2011.06.004.

[6] Delery, J. M., "Experimental Investigation of Turbulence Properties in Transonic Shock/Boundary-Layer Interactions," *AIAA Journal*, Vol. 21, No. 2, 1983, pp. 180–185. https://doi.org/10.2514/3.8052.

[7] Liu, X., and Squire, L. C., "An Investigation of Shock/Boundary-Layer Interactions on Curved Surfaces at Transonic Speeds," *Journal of Fluid Mechanics*, Vol. 187, 1988, p. 467–486. https://doi.org/10.1017/S0022112088000527.

[8] Sandham, N., Yao, Y., and Lawal, A., "Large-Eddy Simulation of Transonic Turbulent Flow Over a Bump," *International Journal of Heat and Fluid Flow*, Vol. 24, No. 4, 2003, pp. 584–595. https://doi.org/10.1016/S0142-727X(03)00052-3.

[9] Bron, O., "Numerical and Experimental Study of the Shock-Boundary Layer Interaction in Transonic Unsteady Flow," Ph.D. thesis, Royal Institute of Technology, Sweden, 2003.

[10] Wollblad, C., Davidson, L., and Eriksson, L.-E., "Large Eddy Simulation of Transonic Flow with Shock Wave/Turbulent Boundary Layer Interaction," *AIAA Journal*, Vol. 44, No. 10, 2006, pp. 2340–2353. https://doi.org/10.2514/1.20358.

[11] Wollblad, C., Davidson, L., and Eriksson, L.-E., "Investigation of Large Scale Shock Movement in Transonic Flow," *International Journal of Heat and Fluid Flow*, Vol. 31, No. 4, 2010, pp. 528–535. https://doi.org/10.1016/j.ijheatfluidflow.2010.02.009.

[12] Brouwer, J., "A Study of Transonic Shock-Wave/Boundary-Layer Interactions Using Conservative, Skew-Symmetric Finite-Differences," Ph.D. thesis, Technische Universitaet Berlin, Germany, 2016.

[13] Priebe, S., Wilkin, I., Daniel, Breeze-Stringfellow, A., Jothiprasad, G., and Cheung, L. C., "Large Eddy Simulation of Laminar and Turbulent Shock/Boundary Layer Interactions in a Transonic Passage," *Turbo Expo: Power for Land, Sea, and Air*, Vol. 2A: Turbomachinery, 2020. https://doi.org/10.1115/GT2020-14244.

[14] Marquillie, M., Laval, J.-P., and Dolganov, R., "Direct Numerical Simulation of a Separated Channel Flow with a Smooth Profile," *Journal of Turbulence*, Vol. 9, 2008, p. N1. https://doi.org/10.1080/14685240701767332.

[15] Laval, J.-P., and Marquillie, M., "Direct Numerical Simulations of Converging–Diverging Channel Flow," *Progress in Wall Turbulence: Understanding and Modeling: Proceedings of the WALLTURB International Workshop held in Lille, France, April 21-23, 2009*, Springer, 2011, pp. 203–209. https://doi.org/10.1007/978-90-481-9603-6_21.

[16] Bernard, A., Foucaut, J.-M., Dupont, P., and Stanislas, M., "Decelerating Boundary Layer: A New Scaling and Mixing Length Model," *AIAA Journal*, Vol. 41, No. 2, 2003, pp. 248–255. https://doi.org/10.2514/2.1937.

[17] Schiavo, L. A., Jesus, A. B., Azevedo, J. L., and Wolf, W. R., "Large Eddy Simulations of Convergent–Divergent Channel Flows at Moderate Reynolds Numbers," *International Journal of Heat and Fluid Flow*, Vol. 56, 2015, pp. 137–151. https://doi.org/10.1016/j.ijheatfluidflow.2015.07.006.

[18] Schiavo, L. A., Wolf, W. R., and Azevedo, J. L. F., "Turbulent Kinetic Energy Budgets in Wall Bounded Flows with Pressure Gradients and Separation," *Physics of Fluids*, Vol. 29, No. 11, 2017, p. 115108. https://doi.org/10.1063/1.4992793.

[19] Bur, R., Benay, R., Galli, A., and Berthouze, P., "Experimental and Numerical Study of Forced Shock-Wave Oscillations in a Transonic Channel," *Aerospace Science and Technology*, Vol. 10, No. 4, 2006, pp. 265–278. https://doi.org/10.1016/j.ast.2005.12.002.

[20] Moroianu, D., Caraeni, D., and Fuchs, L., "Large Eddy Simulation of a Shock Boundary Layer Interaction in a Transonic Internal Flow," *43rd AIAA Aerospace Sciences Meeting and Exhibit*, 2005, p. 312. https://doi.org/10.2514/6.2005-312.

[21] Tucker, P., "Trends in Turbomachinery Turbulence Treatments," *Progress in Aerospace Sciences*, Vol. 63, 2013, pp. 1–32. https://doi.org/10.1016/j.paerosci.2013.06.001.

[22] Bodin, O., and Fuchs, L., "Shock Unsteadiness and Shock Induced Separation at Transonic Flow over a Bump," *38th Fluid Dynamics Conference and Exhibit*, 2008, p. 4174. https://doi.org/10.2514/6.2008-4174.

[23] Reynolds, W., and Hussain, A., "The Mechanics of an Organized Wave in Turbulent Shear Flow. Part 3. Theoretical Models and Comparisons with Experiments," *Journal of Fluid Mechanics*, Vol. 54, No. 2, 1972, pp. 263–288. https://doi.org/10.1017/S0022112072000679.

[24] Brereton, G., and Reynolds, W., "Dynamic Response of Boundary-Layer Turbulence to Oscillatory Shear," *Physics of Fluids A: Fluid Dynamics*, Vol. 3, No. 1, 1991, pp. 178–187. https://doi.org/10.1063/1.857877.

[25] Huynh, H. T., "A Flux Reconstruction Approach to High-Order Schemes Including Discontinuous Galerkin Methods," *18th AIAA Computational Fluid Dynamics Conference*, 2007, p. 4079. https://doi.org/10.2514/6.2007-4079.

[26] Roe, P. L., "Approximate Riemann Solvers, Parameter Vectors, and Difference Schemes," *Journal of Computational Physics*, Vol. 43, No. 2, 1981, pp. 357–372. https://doi.org/10.1016/0021-9991(81)90128-5.

[27] Cockburn, B., and Shu, C.-W., "The Local Discontinuous Galerkin Method for Time-Dependent Convection-Diffusion Systems," *SIAM Journal on Numerical Analysis*, Vol. 35, No. 6, 1998, pp. 2440–2463. https://doi.org/10.1137/S0036142997316712.

[28] Castonguay, P., Williams, D., Vincent, P., and Jameson, A., "Energy Stable Flux Reconstruction Schemes for Advection–Diffusion Problems," *Computer Methods in Applied Mechanics and Engineering*, Vol. 267, 2013, pp. 400–417. https://doi.org/10.1016/j.cma.2013.08.012.

[29] Carpenter, M. H., and Kennedy, C. A., "Fourth-Order 2N-storage Runge-Kutta Schemes," Tech. Rep. No. NASA-TM-109112, NASA, 1994. URL https://ntrs.nasa.gov/api/citations/19940028444/downloads/19940028444.pdf.

[30] Persson, P.-O., and Peraire, J., "Sub-Cell Shock Capturing for Discontinuous Galerkin Methods," *44th AIAA Aerospace Sciences Meeting and Exhibit*, 2006, p. 112. https://doi.org/10.2514/6.2007-4079.

[31] Ducros, F., Ferrand, V., Nicoud, F., Weber, C., Darracq, D., Gacherieu, C., and Poinsot, T., "Large-Eddy Simulation of the Shock/Turbulence Interaction," *Journal of Computational Physics*, Vol. 152, No. 2, 1999, pp. 517–549. https://doi.org/10.1006/jcph.1999.6238.

[32] Goffart, N., Tartinville, B., Puri, K., Hirsch, C., and Pirozzoli, S., "High-Order, High-Fidelity Simulation of Unsteady Shock-Wave/Boundary Layer Interaction Using Flux Reconstruction," *8th European Congress on Computational Methods in Applied Sciences and Engineering*, 2022. https://doi.org/10.23967/eccomas.2022.138.

[33] Wang, C., Zhang, X., Shu, C. W., and Ning, J., "Robust High Order Discontinuous Galerkin Schemes for Two-Dimensional Gaseous Detonations," *Journal of Computational Physics*, Vol. 231, No. 2, 2012, pp. 653–665. https://doi.org/10.1016/j.jcp.2011.10.002.

[34] Klein, M., Sadiki, A., and Janicka, J., "A Digital Filter Based Generation of Inflow Data for Spatially Developing Direct Numerical or Large Eddy Simulations," *Journal of Computational Physics*, Vol. 186, No. 2, 2003, pp. 652–665. https://doi.org/10.1016/S0021-9991(03)00090-1.

[35] Adler, M. C., Gonzalez, D. R., Stack, C. M., and Gaitonde, D. V., "Synthetic Generation of Equilibrium Boundary Layer Turbulence from Modeled Statistics," *Computers & Fluids*, Vol. 165, 2018, pp. 127–143. https://doi.org/10.1016/j.compfluid.2018.01.003.

[36] Xie, Z. T., and Castro, I. P., "Efficient Generation of Inflow Conditions for Large Eddy Simulation of Street-Scale Flows," *Flow, Turbulence and Combustion*, Vol. 81, No. 3, 2008, pp. 449–470. https://doi.org/10.1007/s10494-008-9151-5.

[37] Lund, T. S., Wu, X., and Squires, K. D., "Generation of Turbulent Inflow Data for Spatially-Developing Boundary Layer Simulations," *Journal of Computational Physics*, Vol. 140, No. 2, 1998, pp. 233–258. https://doi.org/10.1006/jcph.1998.5882.

[38] Sartor, F., Losfeld, G., and Bur, R., "PIV Study on a Shock-Induced Separation in a Transonic Flow," *Experiments in Fluids*, Vol. 53, 2012, pp. 815–827. https://doi.org/10.1007/s00348-012-1330-4.

[39] Korakianitis, T., "On the Propagation of Viscous Wakes and Potential Flow in Axial-Turbine Cascades," *Journal of Turbomachinery*, Vol. 115, No. 1, 1993, pp. 118–127. https://doi.org/10.1115/1.2929196.

[40] Sigfrids, T., "Hot Wire and PIV Studies of Transonic Turbulent Wall-Bounded Flows," Licentiate thesis, Royal Institute of Technology, Sweden, 2003.

[41] Schlatter, P., and Örlü, R., "Assessment of Direct Numerical Simulation Data of Turbulent Boundary Layers," *Journal of Fluid Mechanics*, Vol. 659, 2010, pp. 116–126. https://doi.org/10.1017/S0022112010003113.

[42] Poggie, J., Bisek, N. J., and Gosse, R., "Resolution Effects in Compressible, Turbulent Boundary Layer Simulations," *Computers & Fluids*, Vol. 120, 2015, pp. 57–69. https://doi.org/10.1016/j.compfluid.2015.07.015.

[43] Wenzel, C., Selent, B., Kloker, M., and Rist, U., "DNS of Compressible Turbulent Boundary Layers at Varying Subsonic Mach Numbers," *47th AIAA Fluid Dynamics Conference*, 2017, p. 3116. https://doi.org/10.2514/6.2017-3116.

[44] Smits, A. J., and Dussauge, J.-P., *Turbulent Shear Layers in Supersonic Flow*, Springer New York, NY, 2006. https://doi.org/10.1007/b137383.

[45] Welch, P., "The Use of Fast Fourier Transform for the Estimation of Power Spectra: a Method Based on Time Averaging Over Short, Modified Periodograms," *IEEE Transactions on Audio and Electroacoustics*, Vol. 15, No. 2, 1967, pp. 70–73. https://doi.org/10.1109/TAU.1967.1161901.

[46] Clemens, N. T., and Narayanaswamy, V., "Low-Frequency Unsteadiness of Shock Wave/Turbulent Boundary Layer Interactions," *Annual Review of Fluid Mechanics*, Vol. 46, 2014, pp. 469–492. https://doi.org/10.1146/annurev-fluid-010313-141346.

[47] Bruce, P., Babinsky, H., Tartinville, B., and Hirsch, C., "Experimental and Numerical Study of Oscillating Transonic Shock Waves in Ducts," *AIAA Journal*, Vol. 49, No. 8, 2011, pp. 1710–1720. https://doi.org/10.2514/1.J050944.

[48] Rizzi, A., Eliasson, P., Lindblad, I., Hirsch, C., Lacor, C., and Haeuser, J., "The Engineering of Multiblock/Multigrid Software for Navier-Stokes Flows on Structured Meshes," *Computers & Fluids*, Vol. 22, No. 2, 1993, pp. 341–367. https://doi.org/10.1016/0045-7930(93)90065-H.

[49] Pope, S. B., *Turbulent Flows*, Cambridge University Press, 2000. https://doi.org/10.1017/CBO9780511840531.

[50] Krogstad, P.-Å., and Skåre, P. E., "Influence of a Strong Adverse Pressure Gradient on the Turbulent Structure in a Boundary Layer," *Physics of Fluids*, Vol. 7, No. 8, 1995, pp. 2014–2024. https://doi.org/10.1063/1.868513.

[51] Vyas, M. A., Yoder, D. A., and Gaitonde, D. V., "Reynolds-Stress Budgets in an Impinging Shock-Wave/Boundary-Layer Interaction," *AIAA Journal*, Vol. 57, No. 11, 2019, pp. 4698–4714. https://doi.org/10.2514/1.J058487.